INDENTATION SIZE EFFECTS IN RESTRICTED VOLUMES OF MATERIAL

Temur Ahmad

School of Engineering and Material Science

Queen Mary University of London

Supervisors:

Dr Andy Bushby (QMUL)

Dr Xiaodong Hou (NPL)

September 2017

Submitted in partial fulfilment of the requirements of the Degree of Doctor of Philosophy

بسم الله الرحمن الرحيم

الحمد لله رب العالمين،

والصلاة والسلام على رسوله محمد النبي الأمين، وعلى آلهة وصحبه أجمعين،

ومن تبعه بإحسان إلى يوم الدين

Declaration

I, Temur Ahmad, confirm that the research included within this thesis is my own work or that where it has been carried out in collaboration with, or supported by others, that this is duly acknowledged below and my contribution indicated. Previously published material is also acknowledged below.

I attest that I have exercised reasonable care to ensure that the work is original, and does not to the best of my knowledge break any UK law, infringe any third party's copyright or other Intellectual Property Right, or contain any confidential material.

I accept that the College has the right to use plagiarism detection software to check the electronic version of the thesis.

I confirm that this thesis has not been previously submitted for the award of a degree by this or any other university.

Signature:

Date: 23/09/2017

Abstract

Nanomechanics experiments have firmly established the existence of genuine size effects in the strength of crystalline solids that deform by dislocation plasticity. Plastic deformation relieves elastic strain energy when some yield criterion is met. The supply of elastic energy must exceed that required for deformation before plasticity can begin within a given volume of material. An extensive literature is purely geared toward direct compression of pillars using flat punches, while spherical indentation experiments have demonstrated a link between indentation contact size and other length scales, such as grain size. Here we report a new experimental approach in order to test the elastic-plastic response of Nickel, by the introduction of free surfaces to regulate the volume of the potential elastic strained volume and limit that of the plastic volume.

We present results from experiments in a well characterized nickel single crystal, in which pillar-like shapes were machined by focused ion beam milling. A novel method of pillar compression testing is developed in which single crystal nickel pillars are indented using diamond tipped spherical nano-indenters with radii ranging from 3μm to 20μm. The partial-unloading method was used to generate indentation stress-strain curves and identify the onset of plastic deformation. The radius of the indentation contact, a, compared to the diameter of the pillar, D, are varied systematically in the range $a < D < 10a$. The interest lies in the potential coupling of indentation and structure size effects, in which Hall-Petch like behaviour was seen to superimpose on the indentations size effect when the grain size was $< 6a$. Also of interest are the pre-existing dislocation sources within the pre-strained Nickel single crystal, the dislocation dynamics of indenting such pillars and the overall contribution to the mechanical response. The real parameter of interest is the plastic zone size beneath the indentation and its relation to experimentally determined parameters such as contact size.

Acknowledgments

I would like to begin by thanking my wife and best friend, Neelam, whom without the completion of my thesis would not be possible. Her unwavering support and encouragement motivated me to continue after I had lost all will to continue.

I am extremely grateful to my parents for their life-long support and care, there is no success except through their prayers.

I would also like to thank my supervisor, Andy Bushby for recognising my abilities and giving me the opportunity to work towards a PhD, although I have failed in this endeavour the experience I take forward are invaluable.

I have been assisted along the way by many people and would like to thank them for their support. Sofia, Russell and Nadja from Nanovision. Xiaodong and Hannah from NPL. Alex and Chris from CCFE. Harshit from Nanoforce.

I would also like to acknowledge by sponsors EPSRC (QMU_RS_EPSRC) and National Physical Laboratory (NPL) for their financial support.

Contents

List of Figures

List of Tables

Introduction

Nanoindentation testing is the process whereby a material with characterised mechanical properties and geometries is pressed into another material with unknown mechanical properties. Indentation testing is believed to have been derived from Mohr's hardness scale of 1882, in which materials are classified according to their ability to leave scratches on one another. Indentation with spherical shaped tips allows for important mechanical properties such the Elastic modulus, hardness and the yield strength to be derived while only deforming at micro or nano length scales. Bulk mechanical properties can be derived without reaching failure and micro/nano-sized structures can also be characterised with nanometre accuracy. This makes it a non-destructive test method and for this reason it is of great interest for researchers and industry alike.

The indentation size effect is well documented and observed phenomena in the materials science community. What has been observed is that the strength of a material becomes size dependent in the sub-micrometre and nanometre range. The strength of a material increases when the structure is very small or there is a small volume under strain. The size effect has been observed in metals, ceramics, composites and alloys, with varying testing systems such nanoindentation, micropillar compression and tensile testing and wire torsion. When size effects begin to dictate the strength of a material there is a departure from continuum or classical mechanics and our understanding of what derives plasticity is insufficient to explain the size dependence. There is much literature covering this topic and many theories have been postulated to explain this size dependent behaviour and some of the most popular theories will be covered later in this study of the indentation size effect.

This study is concerned with improving our understanding of the indentation size effect by exploring the relationship between the contact size of a spherical indent and the induced plastic

zone. Understanding the nucleation and the evolution of the plastic zone in relation to the contact size could improve our understanding of the indentation size effect. The contact size and plastic zone size relationship could be an important measurable length scale in deriving size dependent strength of materials. This definable parameter could be incorporated into an existing relationship or could form part of a new theory using a renewed understanding of dislocation theory in this size dependent length scale regime.

The aim of this study will be to track the nucleation and evolution of the plastic zone from the onset of plasticity through to higher indentation strains. This will ideally be done for a large range of spherical tips and contact sizes from the nanometre to the tens of micrometre range. Indentation stress-strain data will be generated by limiting the volume of deformable material around the indents to gauge the response to the available elastically strained material. The results of which will be analysed to determine any coupling between the restricted volume and the indentation response for a given contact size. The next stage will be to validate the findings by measuring and/or mapping the plastic zone size through microscopy techniques such as TEM, ECCI and EBSD. The goal is to be able to image the plastic zone size directly underneath indents of varying contact sizes from the onset of plasticity. To then determine any coupling between the contact size and the plastic zone size across the spectrum of length scales and to gain an insight into the dislocation mechanisms at work and their densities within the core and edges of the plastic zone wall.

1. Literature Review

1.1 Hall-Petch effect

The earliest significant work on size effects is perhaps that of Hall (1951) and Petch (1953). Their work demonstrated a variance in mechanical properties with differing magnitudes of grain sizes.

Hall measured the lower yield stresses(σ_{LYP}) of mild steels with differing grain sizes (d) under tensile stress conditions. A plot of σ_{LYP} against grains per linear millimetre clearly shows that there is a lower yield strength dependence on the grain size, i.e. an increase in σ_{LYP} with decreasing grain size (Figure 1).

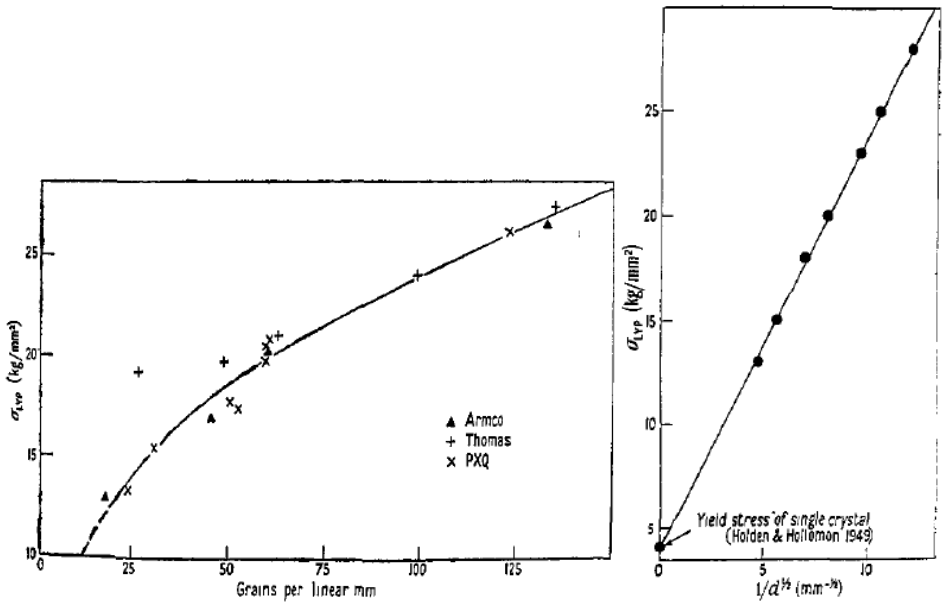

Figure 1: Lower yield strength plotted against grains per linear mm (Hall, 1951) and the linear relationship between the σ_{LYP} and $d^{-1/2}$ (Hall, 1951)

After further analysis of the data Hall found that relationship had a linear fit when the σ_{LYP} is plotted against the inverse square root of the grain size (Figure 1). The line of best fit is

claimed to intercept the y axis at the value for the yield stress of single crystals (Hall, 1951).

The linear relationship is given in the form

$$\sigma_{LYP} - \sigma' \propto \frac{1}{d^{\frac{1}{2}}}$$

(Eq.1.1)

Petch had worked independently of Hall during the same period and had discovered similar observations in his work on tensile experiments on mild steel, ingot iron and spectrographic iron with variable ferritic grain size. The work of Petch was focussed around the sensitivity of steels to fail by brittle fracture that were fine grained in microstructure, the data showed a phenomenon in which the cleavage strength was seen to increase from 25 to 85 tons/sq. over the range of grain size data (Petch, 1953).

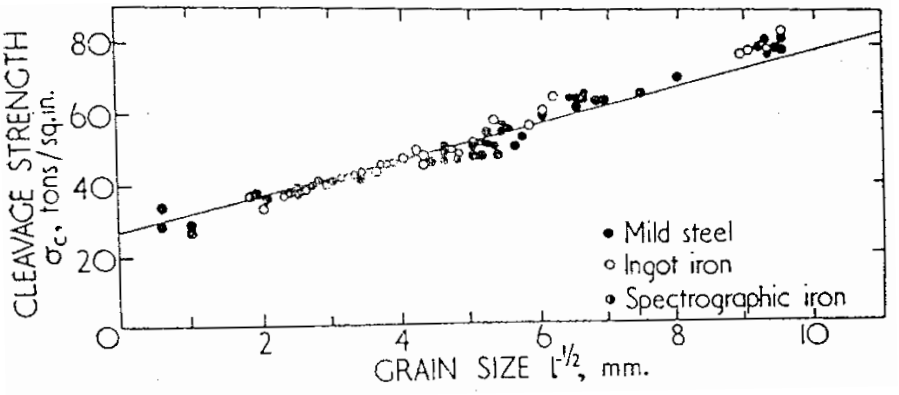

Figure 2: The linear relationship between the cleavage strength σ_c and the inverse square root of the grain size $d^{-1/2}$ (Petch, 1953).

The relationship between the cleavage strength σ_c and the grain size d is again given with a linear inverse square root scaling (Figure 2) in the form

$$\sigma_c = \sigma_0 + kd^{-1/2}$$

(Eq.1.2)

where σ_o and k are constants (Petch, 1953).

Also established experimentally by Petch is the σ_{LYP} scaling linearly with the inverse square root of the grain size $d^{-1/2}$ (Figure 3). The data for all the materials lay on the same line to show good agreement with the work of Hall.

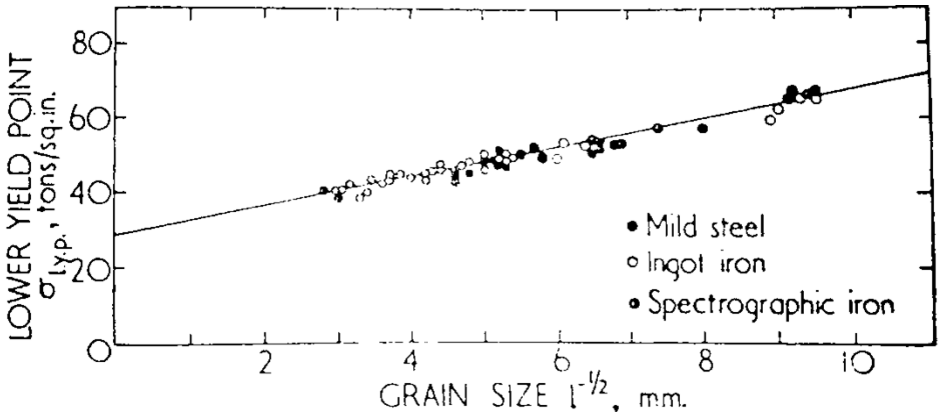

Figure 3: The linear relationship between the lower yield point σ_{LYP} and the inverse square root of grain size $d^{-1/2}$ (Petch 1953).

The grain size dependence of σ_{LYP} also conforms to the observed relationships above by Hall and can be stated as

$$\sigma_{l.y.p} = \sigma_0 + kd^{-1/2}$$

(Eq. 1.3)

1.2 Dislocation Pile-up Model

The first model proposed to explain the Hall-Petch relationship was by Hall himself. The dislocation pile-up model works under the assumptions that the grain boundary acts as a barrier to dislocation motion by having larger yield strength than the grain bulk. This will cause the

dislocations to experience repulsion at the grain boundary interface and pile-up until some critical value of stress concentration has been reached at the tip of the slip band. On completion of this condition, yielding will occur and deformation will proceed on to the adjacent grain (Hall, 1951).

Petch approached the problem from a classical perspective in that he considered the differences in the theoretical strengths and the observed strengths to be the outcome of imperfections, i.e. Griffith cracks. The Griffith cracks model would be used by Petch to analyse the tip of a dislocation pile-up due to the tensile forces experienced at the tip in both circumstances. The high tensile forces produced at the tip of a pile-up is expressed as

$$\sigma = \alpha n \tau$$

(Eq. 1.4)

where σ is the stress, α is a constant, n is the number of dislocations in the pile-up and τ is the shear strength (Petch, 1953).

The model proceeds with Frank-Read sources multiplying on glide planes where they are able to operate until this growth of dislocations causes the process to cease due to the interaction between the dislocations within the build-up. This will be preceded by the pile-up of positive and negative dislocations at the grain boundary acting on both ends of the glide plane, with the maximum value of n arising from a Frank-Read source at the centre of the grain. The dislocations considered so far have been assumed to act independently, however in reality there exists an internal stress field due to the dislocations that exist outside the array. The glide planes with the most densely packed dislocations are subject to a stress by the neighbouring planes which have wider dislocation spacing. This internal stress can be expressed as a shear stress τ_0 that opposes the shear stressτ $(\mathrm{Petch}, 1953)$. Once all the above concerns were taken into consideration it

was empirically shown that the cleavage strength has an inverse square root of grain size dependence (equation 1.3) which also agrees with experimental observations.

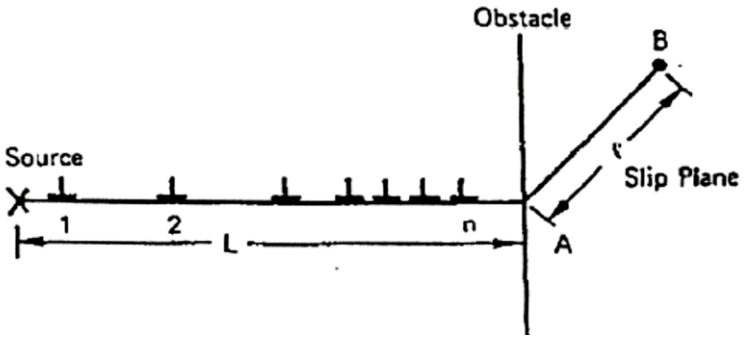

Figure 4: Dislocation pile-up dynamics that give a Hall-Petch relationship (Conrad & Jung, 2005a)

There exist many different types of pile-ups with slightly differing mechanisms at work, which have been analysed from a theoretical stand point. Although the dislocation pile-up model holds true in many cases and in many different forms it is not without its limitations. The reason for this being that there is a lack of direct observations of the occurrence of pile-up at grain boundaries in pure metals with high stacking fault energies (Li & Chou, Y.T, The Role of Dislocations in the Flow Stress Grain Size Relationship, 1970). The theory cannot be said to be the underlying or primary theory involved in grain size strengthening, therefore other models must be applied in circumstances where pile-up is not at work.

1.3 Grain Boundary Source Model

A new theory was required, and a new theory of grain boundary dislocation source was born. Li in his 1963 paper entitled “Petch Relationship and Grain Boundary Sources” also derived a Hall-Petch relationship using this new model by only considering grain boundaries as dislocation

sources without the need for dislocation pile-up. This like for like relationship was shown by considering the example of a simple tilt boundary in which the strength of the partially or fully pinned simple tilt boundary is equal to the stress required to push a dislocation through it, which is given by (Li, 1963a)

$$\sigma_i = \frac{0.45\mu\theta}{2(1-v)}$$

(Eq. 1.5)

where θ is the angle of tilt of the boundary, μ is the shear modulus and v is Poisson's ratio. Using the equation given by Eshelby, Frank and Nabarro for the Hall-Petch slope for dislocation pile-up

$$k = \left[\frac{\sigma_i \mu b l}{\pi(1-v)l_p}\right]^{1/2}$$

(Eq. 1.6)

where l_p is the average length of the pile-up, k is the Hall-Petch slope, l is the grain size and b is the Burgers vector. The Hall-Petch slope for a sub-boundary of this strength is

$$k = \frac{\mu b}{1-v}\left(\frac{0.45 l'\theta}{2\pi b l_p'}\right)^{1/2}$$

(Eq. 1.7)

where l' is the size of the sub-grains and l_p' is the size of the pile-ups in the sub-grains. Stress required to move a dislocation through a Taylor-type forest in which dislocations interact with dislocations on other slip systems from other sub-boundaries is approximately

$$\sigma = \sigma_0 + \frac{\mu b}{2\pi(1-v)}\left(\frac{8\theta}{\pi b}\right)^{1/2} l'^{-1/2}$$

(Eq. 1.8)

A comparable Hall-Petch relationship deduced from pile-up theory (Eq. 1.7) can be reached if the magnitude of the stress in Eq. 1.8 is greater than the following three boundary conditions (Li, 1963a)

1) When $\theta$is small allowing the free dislocations to be separated from the pinned dislocations
2) When θ reaches a critical angle allowing the dislocations to break free
3) If all the dislocations in the tilt boundary are free or have just become free

Li describes a new mechanism dominating when the angle of the grain boundary is high and dislocations can no longer be generated from the sub-boundary, dislocations are now said to originate from grain boundary ledges or jogs which act as donors. In other words, the stress required to generate dislocations from grain boundary ledges must be small for high angle boundary conditions. The ledges are simply thought of as dislocations "absorbed" onto the grain boundaries and their ability to emit dislocations is dependent on the structure and composition of the grain boundary but is thought to be independent of grain size (Li, 1963a) (Li & Chou, Y.T, The Role of Dislocations in the Flow Stress Grain Size Relationship, 1970). A limitation of grain boundary ledges as donors is that once a dislocation has been "desorbed" the grain boundary ledge disappears. This is not sufficient to allow for continuous dislocation multiplication which must occur through another mechanism (Li, 1963b). Li proposed that dislocation multiplication occurs through a combination of cross-slip and Frank-Read sources depending on the frequency of cross-slip and the renewal of the Frank-Read source.

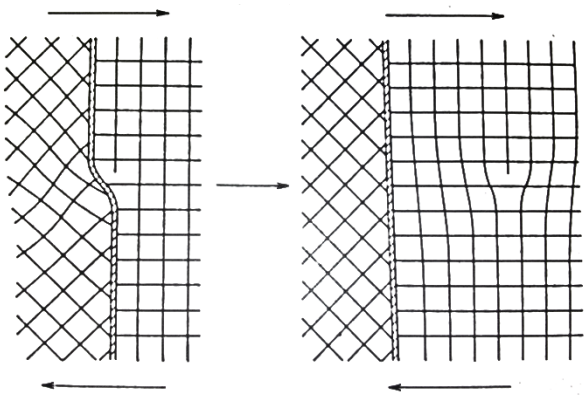

Figure 5: Grain boundary ledge acting as a dislocation donor (Li, 1963b)

The flow stress for this condition at yielding is the stress required to move the dislocations sourced from the grain boundary ledges through a Taylor-type forest. The dislocation density of the forest is

$$\frac{8m}{\pi l}$$

(Eq. 1.9)

where m is the ledge or source density in the grain boundary (number per unit length or length per unit area) (Li, Petch Relationship and Grain Boundary Sources, 1963a).

Giving a flow stress

$$\sigma = \sigma_0 + \alpha\mu b \left(\frac{8m}{\pi}\right)^{1/2} l^{-1/2}$$

(Eq. 1.10)

where α was determined experimentally to be 0.4 and has some dependency on dislocation arrangement. By considering the above a Hall-Petch relationship is derived if the strength of the boundary is assumed to be

$$\sigma_i = 8\alpha^2 \mu b(1-v) m l_p / l$$

(Eq. 1.11)

Which is the approximately the stress required to push a dislocation through the ledge stress field if the ledges form a wall of dislocations (Li, Petch Relationship and Grain Boundary Sources, 1963a).

What has ultimately been demonstrated by Li is the ability to obtain a Hall-Petch relationship without the need for a pile-up model. This is because the stress required to penetrate the grain boundary by pile-up of dislocations is almost equal to the stress required to generate dislocations from grain boundary ledges to form a Taylor-type forest adjacent to the grain boundary.

The structure and geometry of grain boundaries in Nickel and Steel were analysed by Murr using transmission electron microscopy to determine the effect of grain boundary misfit on ledge structure and density. It was found to be that grain boundary ledges do in fact act as a major dislocation source at the onset of yield for metals and alloys and are sensitive to grain mis-orientation with regards to the ledge density (Murr, 1975). Ledge or source density increases with greater grain boundary mis-orientation due to an increase in grain boundary length or area which is said to be in good agreement with the work of Li and Chou.

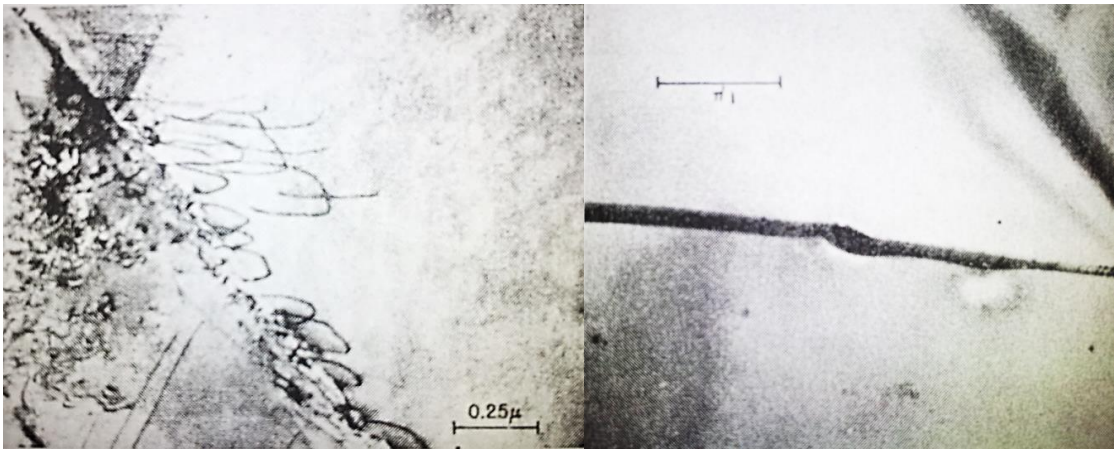

Figure 6: Dislocations emitted from a grain boundary (Li, 1963b) and a grain boundary ledge in Tungsten (S. Weissmann from Li, 1963b)

1.4 Dislocation Density Model

The dislocation density model proposed by Conrad analyses the effects of grain size on the yield and flow stress of metals in which at a given strain the dislocation density is higher for fine-grained specimen than in a coarse-grained specimen due to the result of a smaller free slip length (Conrad, Feuerstein, & Rice, 1967). The flow stress relationship with dislocation density provides the following relationship (Conrad & Jung, 2005b).

$$\sigma = M\alpha_d \mu b \rho^{1/2}$$

(Eq. 1.12)

where σ is the flow stress, M is the Taylor factor, α_d is the total dislocation density, μ the shear modulus, b the Burgers vector and ρ is the dislocation density. Equation 1.12 can be derived to give a Hall-Petch relationship between the shear stress τ and the dislocation density ρ.

$$\tau = \tau_0 + \alpha_d \mu b \rho^{-1/2}$$

(Eq. 1.13)

Regarding the dislocation density model, grain boundaries can participate in increasing dislocation density in the following ways.

a) Grain boundaries act as a dislocation source through grain boundary ledges as proposed by Li.
b) Grain boundaries reduce the average distance dislocations can move for a given strain (Slip-distance theory)
c) Geometrically necessary dislocations (GND'S) occur at grain boundaries to facilitate the inhomogeneous deformation which cause voids and overlapping

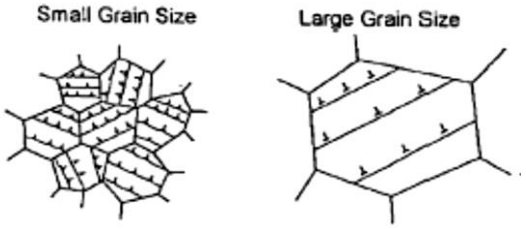

Figure 7: Dislocation free slip distance for small and large grain sizes (Conrad & Jung, 2005a)

The three mechanisms that facilitate dislocation density can quite easily operate in sync with one another, either in complete independence or in any combination (Conrad & Jung, 2005a). Three regimes of grain sizes have been identified in Copper, Silver and Gold with values typically, $d > \sim 0.5\mu m$ for regime 1, $d \approx 10 - 500nm$ for regime 2 and $d < \sim 10nm$ for regime 3. The Hall-Petch equation can be used to show the relationship of the grain size on flow stress for regimes 1 and 2. It has been shown that the governing mechanism in regime 1 is of the dislocation density model, behaviour in regime 2 has been attributed to grain boundary shear due to pile-up of dislocations at grain boundaries. In regime 3 there is expected to be grain size softening attributed to grain boundary shear accommodated by grain boundary diffusion. At the point of transition between regimes there may not exist just a single mechanism of deformation

but a combination of mechanisms working at varying rates (Conrad & Jung, 2005a) (Conrad & Jung, 2005b).

1.5 Geometrically Necessary Dislocation Model

Polycrystalline materials that undergo plastic deformation in a non-uniform manner are subject to strain gradients between different grains. Each grain can be separated into a region of uniform deformation which occurs predominately via single slip. Grains are randomly orientated relative to each other and the difference in strain leads to the formation of overlap and voids between grain boundaries. Overlaps are overcome by dislocations nucleated from the grain boundary and voids through dislocations by the same process but of the opposite sign. These dislocations as proposed by Ashby are said to be geometrically necessary (Ashby, 1970).

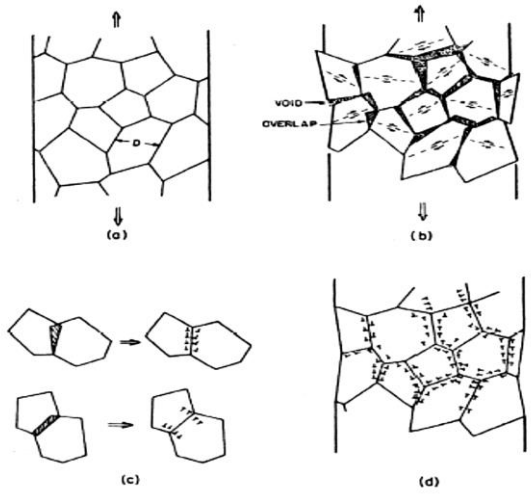

Figure 8: Deformation of a polycrystal leading to the formation of voids and overlaps which are subsequently accommodated by Geometrically Necessary Dislocations (Ashby, 1970)

The density of the GNDs is expressed as

$$\rho^G = \frac{\varepsilon}{4bd}$$

(Eq. 1.14)

where $\boldsymbol{\varepsilon}$ is the tensile strain, b is the Burgers vector and d is the grain size.

The total dislocation density is made up of both GNDs which are a characteristic of the microstructure and statistically stored dislocations (SSDs) which are a characteristic of the material itself.

$$\rho_T = \rho_G + \rho_S$$

(Eq. 1.15)

The strengthening mechanism arises through the storage of GNDs and SSDs and their geometric slip distance which in the case of the GNDs is related to the grain size. The dislocations are either stored to accommodate for deformation gradients within the specimen or become trapped by one another in a random way (Ashby, 1970). As the GNDs are created to accommodate for lattice curvature by acting as storage for extra defects in the lattice they are not contributing to plastic strain but act to work harden the material by acting as obstacles to the motion of SSDs. i.e. SSDs work to relieve the stress by glide and GNDs align themselves to accommodate the strain gradients (Gao & Huang, 2003). The type of hardening that may be experienced is dependent on the weather a moving dislocation is interacting with a GND or a GND with a mobile dislocation. In the first case, there is jog formation as the GND causes the mobile dislocation to move out of the glide plane leading to macroscopic isotropic hardening. In the latter case, there is kinematic hardening. Hardening through these dislocation interaction mechanisms is further heightened through the build-up of back stresses (Fleck, Ashby, & Hutchinson, 2003).

1.6 Inverse Hall-Petch/Grain Size Softening

Nanocrystalline materials composed of grain sizes in the region of 1-100nm are showing much promise in a range of applications due to their unique properties, namely the high strength they are expected to show from the classical Hall-Petch behaviour which gives the following expression

$$\sigma_y = \sigma_0 + kd^{-1/2}$$

(Eq. 1.16)

where σ_0 is the friction stress required to move individual dislocations, k is a constant and d is the grain size. The data for grain size strengthening follows a positive k slope with a $d^{-1/2}$ scaling against yield strength σ_y. Therefore, a reduction in grain size should produce an increase in the yield strength for a given material.

However, the behaviour of nanocrystalline materials deviates from this predicted behaviour at grain sizes <20-50nm for many materials. What can often be seen at this stage is termed grain size softening in which there is either a reduction in the yield strength or a plateauing of the yield strength of the material. Although the inverse Hall-Petch effect (IHPE) is well observed experimentally there currently exists no single model to explain the behaviour as they are thought of as inadequate. Amongst the models proposed the most popular are based upon dislocation behaviour within nanocrystalline materials, Coble creep, grain boundary sliding, two-phase based models and grain boundary triple junction activity (Conrad & Narayan, On the Grain Size Softening in Nanocrystalline materials, 2000) (Carlton & Ferreira, 2007).

The first known experimental observation of the IHPE was by Chockshi et al, 1989, in which the authors had carried out harness tests on Copper and Palladium samples using a Vickers diamond

pyramid indenter. The results for the coarse-grained Copper and nanocrystalline Copper and Palladium is summarised below.

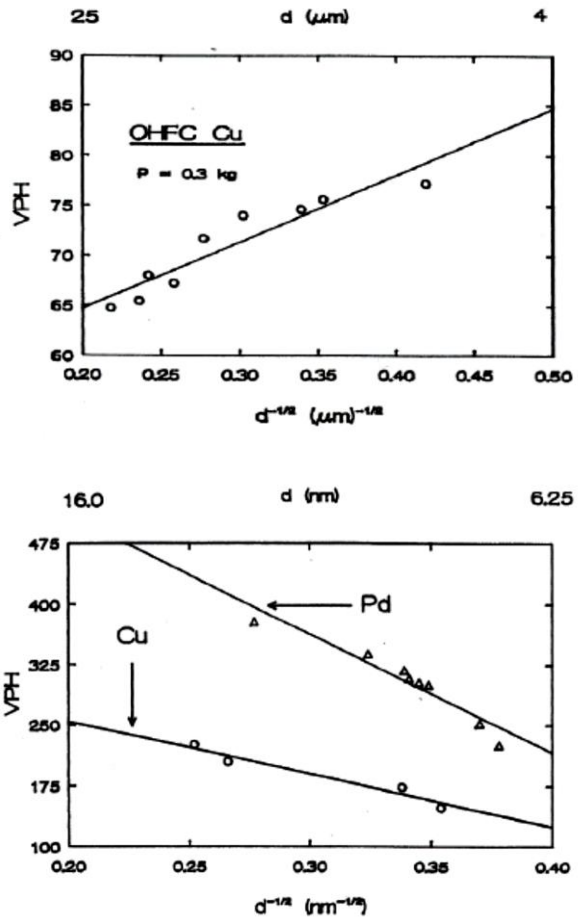

Figure 9: Variation in Vickers Hardness with grain size $d^{-1/2}$ for coarse grained Copper and the Variation in Vickers Hardness for nanocrystalline Copper and Palladium (Chokshi, Rosen, Karch, & Gleiter, H, 1989)

The data clearly demonstrates a positive fit to the data for a Hall-Petch relation in the case of the coarse-grained Copper whereas the nanocrystalline Copper and Palladium show a negative Hall-Petch slope for the same Vickers hardness against the inverse square-root of grain size parameters. The reason for such behaviour has been attributed to the onset of diffusional creep by the transport of vacancies along grain boundaries (Coble Creep) and by grain boundary sliding. (Chokshi, Rosen, Karch, & Gleiter, H, 1989). In subsequent research it was shown through

measurements of creep rates of Copper and Palladium that in fact there is no difference in the creep rates of nanocrystalline and coarse-grained materials. The grain size softening of Copper and Palladium was attributed to the annealing history of single specimens through analysis of the experimental procedures of others which showed a correlation between those that had observed the IHPE and those that hadn't (Weertman, 1993). In other words, the IHPE was only observed in specimens that had been repeatedly annealed to modify the grain sizes for later use as part of the same study.

Conrad and Narayan proposed a model which draws on the findings of computer simulations in which it was seen that dislocation activity ceased in Copper and Nickel when the grain size reached a critical value of ≈10nm. The deformation after this critical grain size proceeds via grain boundary shear. This thermally activated shear rate is expressed as

$$\dot{y} = N_v A b v \, exp\left[\frac{-\Delta G_{(\tau_e)}}{kT}\right]$$

(Eq. 1.17)

where N_v is the number of places per unit volume where thermally activated shear can occur, A is the area swept out per thermal fluctuation, b the atomic diameter, v the frequency of vibration and $\Delta G_{(\tau_e)}$ the Gibbs free activation energy, which is a decreasing function of the effective shear stress (Conrad & Narayan, 2000). Adding some suitable expansion parameters to equation 1.17 gives

$$\dot{y} = \frac{6 b v_d}{d} sinh\left(\frac{v\tau_e}{kT}\right) exp\left(-\frac{\Delta F}{kT}\right)$$

(Eq. 1.18)

The derived values for v and ΔF are in agreement with the values the authors had expected which, led them to conclude that the deformation behaviour for nanocrystalline metals below the critical grain size $d < d_c$ is driven by grain boundary sliding by single atomic shear events. Grain boundary sliding is said to become more energetically favourable at this critical grain size, however there is expected to be a region in which both dislocation motion and grain boundary sliding mechanisms are at work. The reason for this being that the presented model holds true for an idealised nanocrystalline material in which the grain size is uniform with a random orientation, while being relatively free of porosity and other imperfections (Conrad & Narayan, 2000).

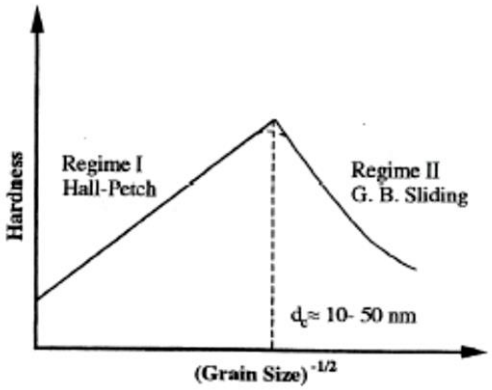

Figure 10: Variation of hardness wit he Grain size $d^{-1/2}$ with variation in mechanisms (Conrad & Narayan, On the Grain Size Softening in Nanocrystalline materials, 2000)

Carlton and Ferreira considered a grain boundary to have a specific activation energy for dislocation absorption and they also demonstrated that a dislocation has a certain probability of being absorbed onto the grain boundary. The probability of a dislocation being absorbed by the grain boundary is P_{dis} and the probability of a dislocation core making the jump is P_{atom}, p denotes a dislocation making a successful jump into the grain boundary on the first attempt and (1-p) is the probability of a dislocation not making it on a first attempt. This gives the equation

$$P_{dis} = P_{atom}^{J} = [1 - (1 - p)^{N}]^{J}$$

(Eq. 1.19)

where J is the total number of atoms on the dislocation core jumping into the grain boundary, J is determined by multiplying the atomic linear density of the dislocation core by the length l of the dislocation line. N is the number of attempted jumps by dislocation core atoms to the grain boundary during time $\bar{t}$ between absorption of dislocations (Carlton & Ferreira, 2007). Taking into account the crystallographic structure of the grain boundary gives

$$P_{dis} = \{1 - [1 - e^{M}]^{N}\}^{J}$$

(Eq. 1.20)

where M is a mobility factor. Equation 1.20 demonstrates that as the number of attempted jumps to the grain boundary by dislocation core atoms increases so too does the probability of a dislocation being absorbed by the grain boundary. This leads to the consideration of weather grain boundaries can absorb dislocations fast enough at reasonable strain rates (Carlton & Ferreira, 2007). This conclusion can be evaluated by considering the strain rate associated with the motion of a single dislocation passing through a single grain at an average time $\bar{t}$.

$$\dot{\varepsilon} = \left(\frac{\bar{x}}{d}\frac{b}{d}\right)/t$$

(Eq. 1.21)

$\bar{x}$ is the average distance moved by a dislocation during time t. The average time taken for each dislocation to cross the entire grain is

$$\bar{t} = \frac{b}{(\dot{\varepsilon}d)}$$

(Eq. 1.22)

Carlton and Ferreira have concluded from this that the greater the degree of grain boundary absorption the larger the deviation from Hall-Petch behaviour there is. Classical Hall-Petch behaviour is derived from dislocation pile-up at a rigid grain boundary where there is no absorption of dislocations into the grain boundary, i.e. P_{dis}= 0. But when $P_{dis} \neq 0$ the shear stress on the leading dislocation at the head of a pile-up of n dislocations is equal to the back-stress due to the contribution of the internal stresses produced by the grain boundary. Expressed as

$$\tau_1 = \tau_0 = \frac{n\tau}{(1 - P_{dis})}$$

$$\tau^2 = \frac{\tau_1 \mu b(1 - \mu_{dis})}{d}$$

(Eq. 1.23)

where τ_0 is the internal stress, d is the grain size, b is the Burgers vector and μ is the shear modulus.

Applying the Schmid factor to equation 1.21 gives

$$\sigma = \left[\frac{\sigma_1 \mu b}{cos\theta cos\vartheta}\right]^{1/2} \left[\frac{1 - P_{dis}}{d}\right]^{1/2}$$

(Eq. 1.24)

Taking the first half of the equation to equal k and including a value for the lattice friction stress $\sigma_0 = 0$ gives a modified Hall-Petch relationship

$$\sigma_y = \sigma_0 + k\left[\frac{1 - P_{dis}}{d}\right]^{1/2}$$

(Eq. 1.25)

The model of dislocation absorption acts to reduce the number of dislocation in the pile-up thus reducing the stress concentration the tip. The value of P_{dis} is negative which means that the

Hall-Petch slope k is an inversion of the classical Hall-Petch relationship. The above model by Carlton and Ferreira has many limitations not least in the fact it is very difficult to fit to the published data due to the parameters such as strain rate used and due to the experimental procedures employed.

1.7 Does the Hall-Petch relationship really scale with $D^{-1/2}$?

The work of Hall and Petch is generally regarded as a sound basis from which all other size effect phenomena can be approached in as much that the size effect scaling is a power law scaling between 0.2 and 1 depending on the intrinsic characteristics of a material. The Hall-Petch dependence of strength on grain size gives an inverse square root scaling.

$$\sigma = \sigma_0 + \frac{k_{HP}}{\sqrt{d}}$$

Eq. 1.26

The above equation is more commonly expressed in terms of a flow stress σ power law scaling with the length scale l

$$\sigma = \sigma_0 + kl^{-x}$$

Eq. 1.27

where σ_0, k are material constants and x is the size effect scaling exponent.

There exists a mass of data which seems to support the finding that the scaling exponent varies for different classes of materials. The basis for a scaling exponent of $x = \frac{1}{2}\ or\ x = 1$ is derived from first principles. Taylor's equation for the shear flow stress in forest hardening (Eq. 1.28) naturally evokes an inverse square root scaling as does Griffith's equation for crack growth and propagation (Eq. 1.29).

$$\tau = \tau_0 + \alpha\mu b\rho^{1/2}$$

Eq. 1.28

Where α is a proportionality constant of the order of unity, μ is the shear modulus, b is the Burgers vector and ρ is the dislocation density.

$$\sigma_f = \left[\frac{G_c E}{\pi a}\right]^{1/2}$$

Eq. 1.29

Where σ_f is the fracture stress, G_c is the critical energy release rate i.e. fracture toughness, E is the Young's Modulus of the material and a is the size of the flaw. The foundation for the l^{-1} scaling considers the line tension or energy per unit length.

The Hall-Petch equation with an inverse square root scaling has generally been the accepted method for defining grain size strengthening. The theory strengthened with theoretical support has largely gone unchallenged. This raises the question that had the Hall and Petch approached the problem with a theoretical approach of l^{-1}would we have a different understanding of mechanical size effects.

Dunstan and Bushby have revealed how the methods used to extrapolate the scaling exponent have in fact been misleading as the authors have not considered what else does and does not fit the data. "*Good fits of a model to data do not, of themselves, support the model*" (Dunstan & Bushby, 2013). Data from a wide range of experimental techniques was plotted on a graph of Elastic strain ε_E against the effect size $a_0^{-1} l_{eff}$. It is considered preferable to compare materials in terms of elastic strain rather than stress as plasticity occurs through the generation and operation of dislocation. The stress to operate dislocation sources is highly dependent upon the elastic constants, the effective Burgers vector and the constraint of the dislocation curvature which is dependent on the elastic strain.

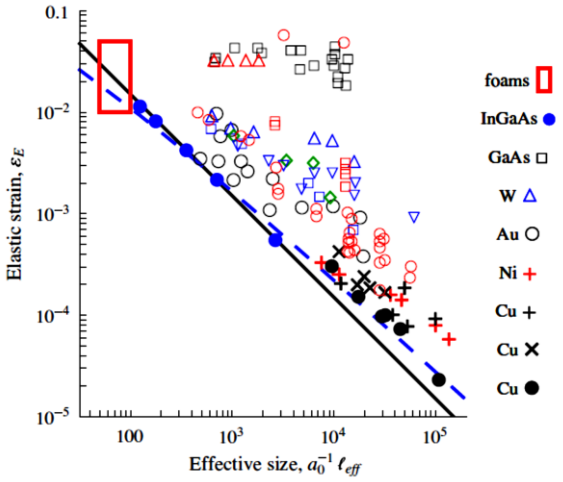

Figure 11: Data from pillar compression, InGaAs layers, tension, torsion and flexure experiments is plotted for the effective size $a_0^{-1}l_{eff}$ against elastic strain ε_E (Dunstan & Bushby, 2013)

It becomes immediately apparent that the data lies on or above the line -1 which has the equation

$$\varepsilon_y = 1.5 l_{eff}^{-1} + G^{-1}\tau_0$$

Eq. 1.30

The line has been termed as the minimum strength which is the addition of the size independent bulk strength and the size dependent strength. This line for minimum strength by no means limits or seeks to describe other strengthening mechanisms but can be interpreted as a base by which other mechanisms act in addition. Dislocations operate via nucleation sources as well as through multiplication, motion and dislocation interactions. All of which result in strengthening effects and in addition to what has been proposed, so it is theoretically sound to assume a minimum strength (Li, Bushby, & Dunstan, 2014). From this underlying principle, the reason for the weaker size effect in stronger materials can be deduced because the size dependent contribution does not dominate until much smaller length scales. Dunstan and Bushby further argue that the scaling exponents may be irrelevant and may not provide any useful information as there is no theoretical justification for it and what is in fact represented by the exponent is some length scales and the bulk strength. The above equation helps us to understand the

underlying principle of the size effect with an exponent of $x = 1$, while other theories are additive in application to the minimum strength. What is of the most significant interest is that the data plotted is from torsion and flexure experiments for which the size effect is most commonly attributed to strain gradients. According to the authors there is strong evidence to suggest that there is a commonality in the size effect at the yield point for all micromechanical experiments (Dunstan & Bushby, 2013).

Based upon previous analysis of the data Dunstan and Bushby propose a fixed exponent of $x = 1$ and a fixed value for k.

$$\sigma = \sigma_0 + kl^{-1} \text{ and } \sigma = \sigma_0 + k\ln ll^{-1}$$

Eq. 1.31 and 1.32

To test the hypothesis that there is in fact a common origin in the size effect, Dunstan and Bushby aim to demonstrate whether the size effect seen in grain size dependence on flow stress is a unique phenomenon or whether it is another manifestation of the size effect seen in other forms of micromechanical testing.

Data from the literature with a range of exponent values from 0.2 to 1 is plotted on a graph with the flow stress $\left(\frac{\sigma_f}{\sigma_f^{max}}\right)$ against the grain size $\left(\left[\frac{d}{d_{min}}\right]^x\right)$ with some scaling exponent x, $-\frac{1}{4}, -\frac{1}{2}\ and -1.$

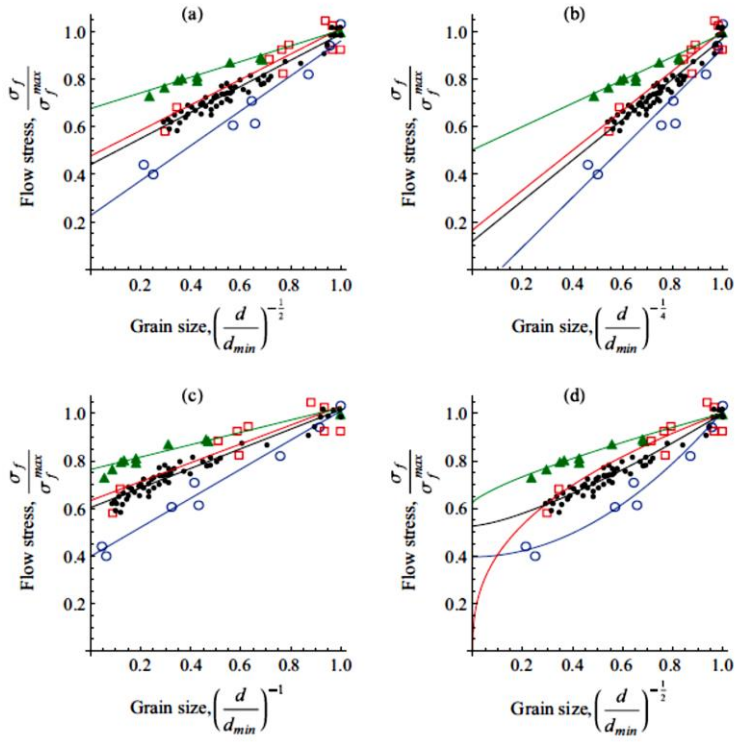

Figure 12: Scaled data demonstrating the Hall-Petch effect for W (open circles), for Fe (small points), for Cu (solid triangles) and brass (open squares). Each data set is called by its minimum grain size and maximum flow stress so they maybe compared on the same axis. Data is plotted against the inverse square-root and the solid lines are a best fit to equation 1.26, (b) and (c) data is plotted against the inverse fourth-root and the solid lines are a best fit to equation 1.27, (d) the data is plotted as in (a) but compared with non-linear fits to equation 1.2 with free fitting parameters.

Fits to the data for all the considered scaling exponents is as equally acceptable and would appear to agree, but this clearly cannot be the case. This further expounds the idea that deriving principles from this type of data analysis is clearly flawed and this classical data in this form gives no real insight into the underlying principle of the size effect and no support for an inverse square root scaling relationship. What is also highlighted is that the actual range of data for the grain sizes is inadequate and more data would be required to confidently reveal the scaling exponent with a straight-line fit (Dunstan & Bushby , 2014).

Dunstan and Bushby then advance to test the validity of the equations with a fixed scaling parameter of $x = -1$.

$$\sigma = \sigma_0 + kl^{-1}$$

Eq. 1.31

$$\sigma = \sigma_0 + k \ln l l^{-1}$$

Eq. 1.32

Further analysis by plotting the normalised stress which is the elastic strain $\varepsilon = \frac{\sigma}{Y}$ against the normalised grain size $\frac{d}{a_0}$ and fitting the normalised data to equations 1.26-1.27 and 1.31-1.32 gives the parameters ε_0, k and x. This is done to better evaluate the credibility of equations 1.31 and 1.32 as they are derived from the relationship between dislocation curvature and stress. The elastic energy relieved through dislocation dynamics is strongly associated with the elastic moduli and the Burgers vector which scales with lattice parameter of the material.

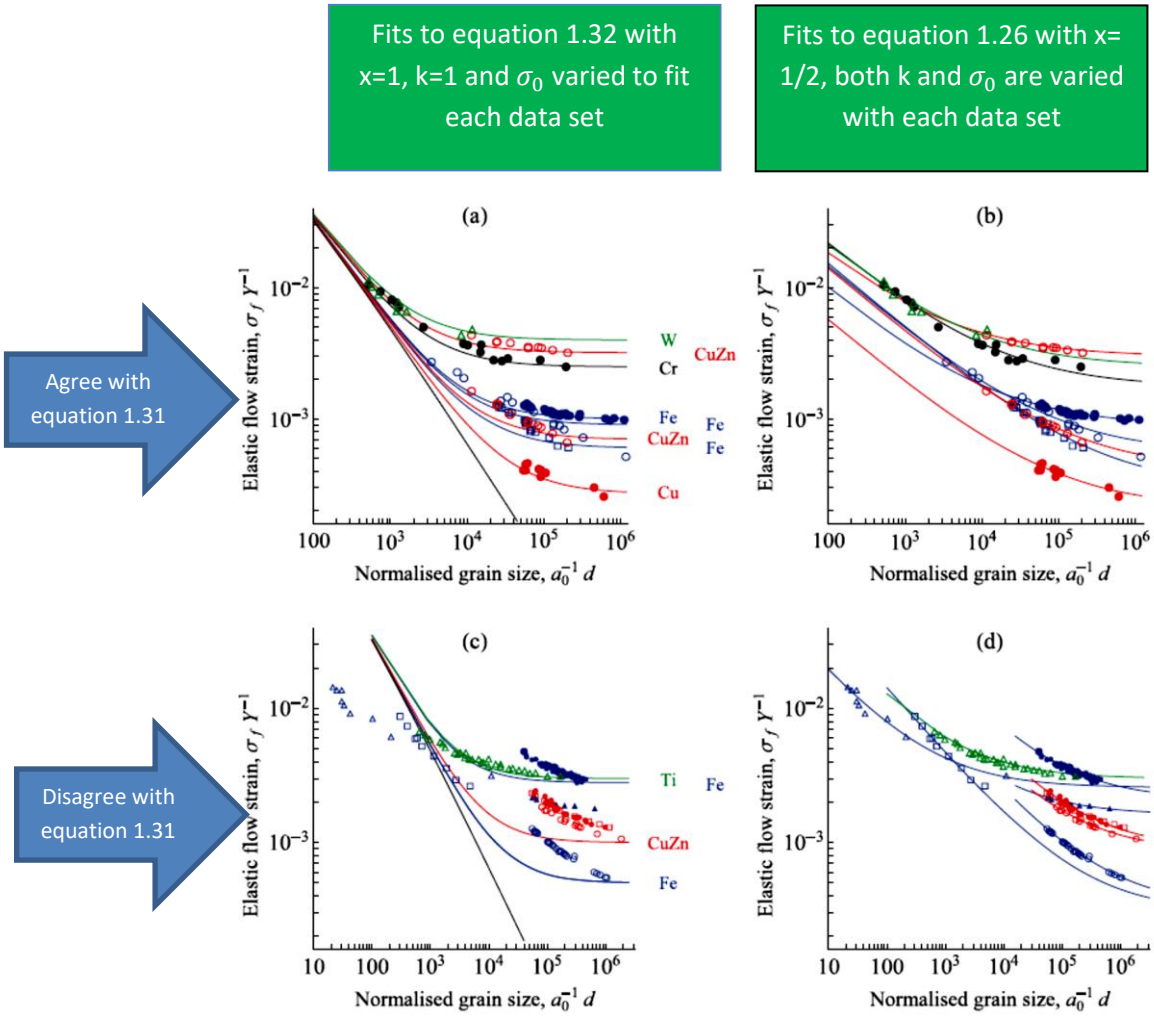

Figure 13: Normalised data for the flow stress or hardness (Dunstan & Bushby , 2014).

The sets of data which agree reasonably well with equation 1.31 are plotted on logarithmic axes in figures 13a and 13b with fits to equation 1.32 and the Hall-Petch formula (equation 1.26) respectively. The solid lines in figures 13a and 13c are fits to equation 1.32 and not the data using a single fitting parameter k and varying value of σ_0 to keep the fit in line with the data. The remaining data is plotted in figure 13c for comparison with equation 1.32 and in figure 13d for comparison with equation 1.26. The unsuitability of equation 1.31to predict the size effect (figures 13c and 13d) suggests that there could be other mechanisms at work that cause the data to deviate from the behaviour expected by equation 1.32. The authors argue that with a size effect exponent of x=-1 (figure 13a) much of the values of k for many materials fall into a single value of $k \sim 1$ meaning that equation 1.32 is sufficient to describe the general response. However, it is inadequate in predicting behaviour where other mechanisms may be contributing to the size effect. This leaves a single fitting parameter σ_0 for each specimen which "*expresses its different asymptotic limit (yield or flow strength at infinite grain size)*" (Dunstan & Bushby , 2014).

1.8 Indentation Size Effect

Early observations of the indentation size effect (ISE) were not completely understood and therefore were scrutinised as flaws in the experimental procedures. The size effect was attributed in particular to surface effects such as hardened surface layers due to polishing, surface roughness which greatly affects results at smaller indenter sizes and the formation of oxides. The apparatus used to measure the indentation response was also seen to be at fault due to indenter tip blunting which leads to a transition from self-similar to spherical geometry, also the methods by which the indent size is measured (Pharr, Herbert, & Goa, 2010).

However continued study of the ISE has shown there exists strong experimental observations for a size effect in relation to the geometry of pointed self-similar indenters such as the Vickers and the more commonly used Berkovich indenter. The hardness of a material is seen to vary with the depth and size of the indent of contact for a geometrically self-similar indenter. The hardness increases at shallower depths of contact (Ma & Clarke, 1995) (Nix & Gao, 1998) (Lim & Chaudhri, 1999) (Swadener, George, & Pharr, 2002) until it reaches some macroscopic value at which it is becomes constant, typically >5μm depending on the type of material and its fabrication history.

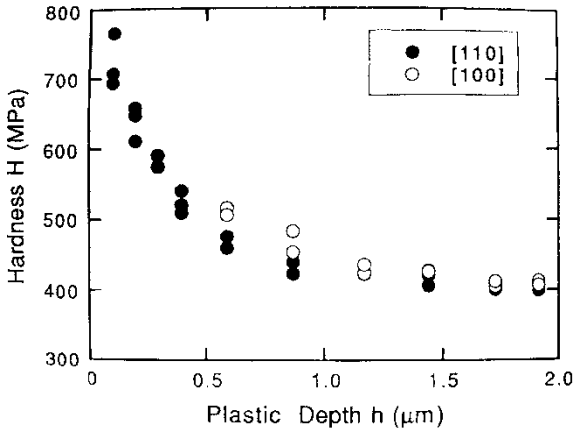

Figure 14: Hardness as a function of plastic depth for silver single crystals of two crystallographic orientations (Ma & Clarke, 1995).

Ma and Clarke, 1995 have given a hardness dependence on the indentation size, D, for a Berkovich indenter in the form of

$$H = \alpha + \beta \frac{8\sqrt{3}}{3D^2}\left[(1+\sqrt{3})D - d\right]$$

(Eq. 1.33)

where α and β are constants and d is the diameter of the rounded tip of the indenter. And for a Vickers indenter the hardness is expected to scale with

$$H = \alpha + \beta \frac{4}{D^2}\left[(1+\sqrt{2})D - d\right]$$

(Eq. 1.34)

A model for the depth dependence of hardness for Cu and Ag has been derived by Nix and Goa, 1998 to give the relationship

$$\frac{H}{H_0} = \sqrt{1 + \frac{h^*}{h}}$$

(Eq. 1.35)

where H is the hardness for a given depth h, H_0 is the macroscopic hardness at infinity and h^* is a characteristic length scale that is dependent on the shape of the indenter, the shear modulus and H_0. The relationship shows linear behaviour for single crystal and polycrystalline samples of Cu and for the data collected by Ma and Clarke on single crystal and polycrystalline silver.

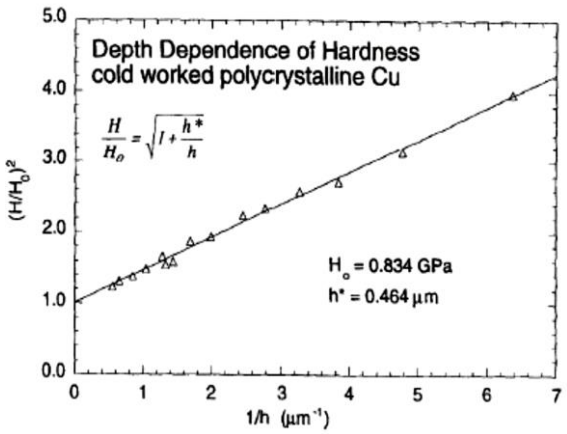

Figure 15: Depth dependence of hardness for polycrystalline Cu plotted according to equation 1.35.

Both sets of authors invoke a model based on geometrically necessary dislocations which accommodate strain gradients at plasticity. The model seems to fit well with experimental data when plotted with strain gradient plasticity but in some cases, it is not applicable (Lim & Chaudhri, 1999). This is due to the fact is does not consider the geometry of the indenter and

the concentration of dislocation density at the surface which were in contact with the sharp internal edges of the indenter, an area of localised strain (Ma & Clarke, 1995).

Unlike the depth dependence of the self-similar geometry indenters, spherical indenters also experience a size effect, one that is related to the indenter radius. The indentation size effect for a spherical indenter was first reported by Lim et al, 1998 using both nano-indentation and micro-indentation on oxygen-free Copper (99.00% purity). Although the spherical radii used ranged from 7µm to 500µm, a scaling effect was only observed for the smallest indenters (7µm and 35µm) for which there was an upward scaling of the mean pressure. This behaviour was considered to be the result of an indenter-grain boundary interaction which is responsible for the plasticity dynamics under the indenter.

It has been shown that there is an increase in the yield pressure of ceramics and metals proportional to the inverse square root of contact radius $a^{-1/2}$ or the inverse cube root of indenter radius $R^{-1/3}$ (Zhu, Bushby, & Dunstan, 2008a) (Zhu, Hou, Bushby, & Dunstan, 2008b). This agrees with the finite element modelling findings of Spary et al, 2006 who found that the indentation size effect is a geometrical effect in which the magnitude of the size effect is dependent on the indenter radius, with a scaling of $R^{-1/3}$ for the yield stress.

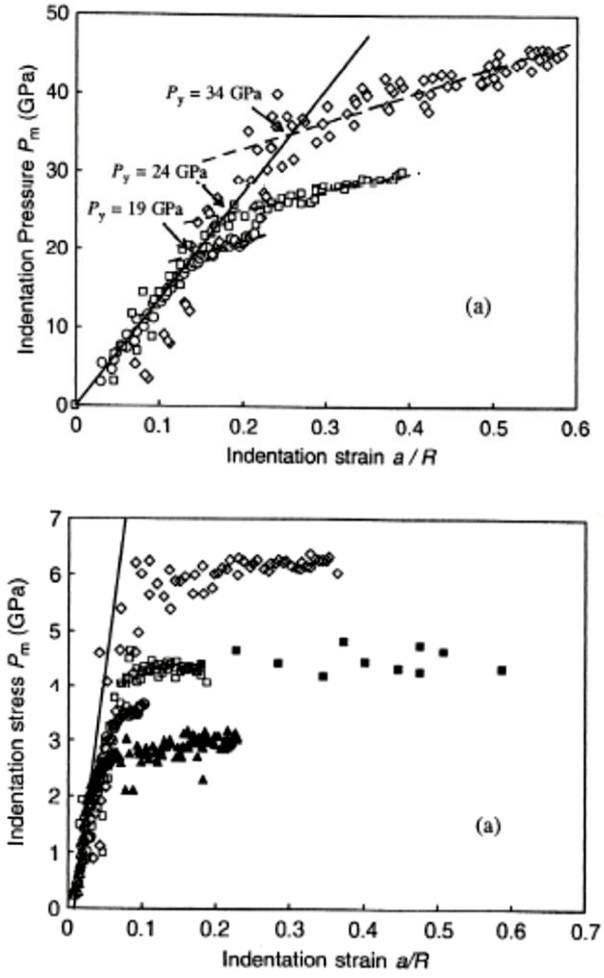

Figure 16: Al_2o_3 indented with spherical radii of 0.5µm (◊), 3µm (□) and 10µm (○). The graph shows the yield pressures for each indenter with the solid line showing a theoretical elastic line and the dotted line is a regression fit for that plastic part (Zhu, Bushby, & Dunstan, 2008a). Tungsten indented with spherical radii of 3µm (◊), 10µm (□), 30µm (○) and 90µm (Δ) where the contact area has been calculated. For the indentations with spherical radii of 7µm (■) and 90µm (▲) the contact radius has been directly measured (Zhu, Bushby, & Dunstan, 2008a).

The upward scaling of the yield pressure for ceramics and metals with smaller spherical indenter radii has been shown by Zhu et al for any given grain size. What is of interest is that when the data for the yield pressure for both the metals and ceramics are normalised by the macroscopic yield pressure (P_y/P_0) the values for metals and ceramics fall on separate linear slopes. This suggests that the magnitude of the size effect for ceramics and metals is different and may be dependent on some/one intrinsic property of the class of material.

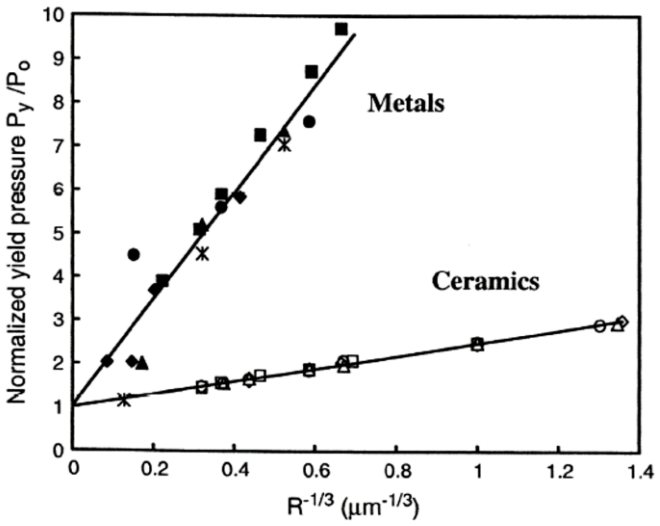

Figure 17: Normalised yield pressures (P_y/P_0) are plotted for $R^{-1/3}$ for metals W (■), Al (▲), Cu (*), Ni (●), Ir (♦) and ceramics Al_2O_3, $In_{0.53}Ga_{0.47}As$ (Δ), GaSb (□), InP (◊) (Zhu, Bushby, & Dunstan, Size Effect in the initiation of plasticity for ceramics and metals, 2008a)

1.8 Interaction between intrinsic and two/three dimensional extrinsic constraints

It has been clearly demonstrated through experimental observations that there exists an indentation size effect (ISE) in both metals and ceramics composed of polycrystalline and single crystal grain sizes. Hou et al investigated the interaction between the grain size and the contact radius on single crystal and polycrystalline copper. For grain sizes, much larger than the indentation size the indentation pressure remains constant until the indentation size reaches some critical value in respect to the grain size. A Hall-Petch relationship ($d^{-1/2}$) is only evident once an approximate ratio of d/a =6 is realized between the grain size and the indentation size. The linear increase in the indentation pressure is due to the additional stress required to induce the same indentation strain. It is at this point where the indentation size is significant to the grain size that there is an increased grain boundary contribution on the indentation pressure before which the indentation pressure was dominated by the indentation size. An attempt is

made to combine the ISE and the grain size effect empirically in quadrature with a new fitting parameter, D expressed as

$$\left(\frac{1}{\sqrt{D}}\right)^2 = \left(\frac{K_1}{\sqrt{a}}\right)^2 + \left(\frac{K_2}{\sqrt{d}}\right)^2$$

(Eq. 1.36)

where K_1 and K_2 are constants and D has units of length. The method works well for Copper and gives a linear scaling of $D^{-1/2}$ for P_m=0.25 for a range of indenter radii between 3µm and 500µm, however is yet to be proven for any other material. This work does demonstrate the significance of the interaction between the ISE and the H-P effect on the flow stress and implies an underlying principle between the two length scales of which smallest will dominate.

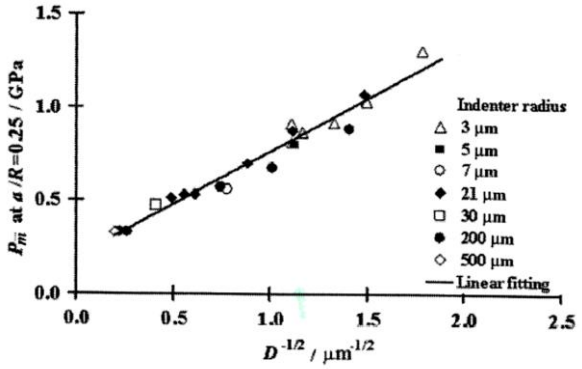

Figure 18: Indentation pressure at a/r=0.25 for different radius indenters against the inverse square root of the fitting parameter D. The data gives a linear fit when a value of K_2=1.5K_1.

A similar occurrence in which the smallest length scale dominates has also been discovered in compression tests on single crystal tungsten pillars (Jennett, Ghisleni, & Michler, 2009). The yield strength was found not to be dependent on aspect ratios, surface to volume ratios or cross-sectional area but purely on the smallest dimension which follows an inverse square root of width relationship.

Foil flexure experiments (Ehrler, et al., 2008) on nickel in which the grain sizes (d) ranged from less than foil thickness (h) to more than foil thickness (h) have shown that the effect of defining the limiting experimental parameters has the same result on the strength. In the case of d>h dislocation motion will generally be hindered through interaction with the free surface, whereas for the condition d<h dislocations are more likely to encounter a grain boundary before encountering the free surface. Therefore, the size effect is driven by the smallest length scale which delimits the strained volume, which may be via the grain boundary according to classical Hall-Petch or through the free surface.

1.9 Slip-distance Theory

In the following case the authors (Bushby et al, 2009) have shown that the indentation size effect is driven by the geometry of contact and scales by the contact size ($a^{-1/2}$) for both Berkovich and spherical indenters as the data falls on a single line regardless. Normalising the yield pressure by $\left(\frac{P_y - P_0}{P_0}\right)$ and plotting as a function of $a^{-1/2}$ reveals that the magnitude of the indentation size effect scales differently for ceramics and metals. The distinct difference in properties between the two classes is the effective Burgers vector and their yield strains. Normalising the yield pressures further by $\frac{\sqrt{\varepsilon_y^{pl}}}{\sqrt{b}}$ leads to all the data falling onto a single line. Slip distance theory is used to account for this behaviour by analysing the slip distance of a dislocation within the plastic zone.

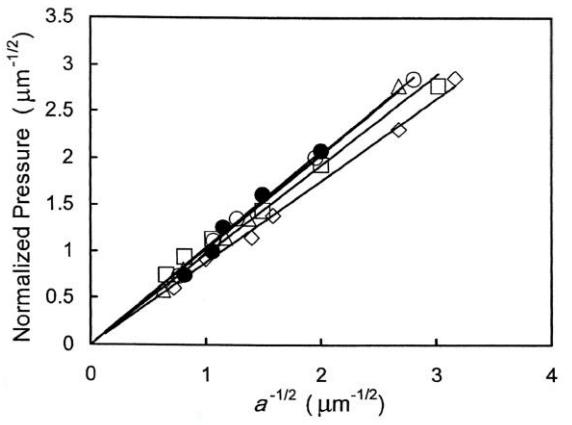

Figure 19: Normalised yield pressure plotted against 1/√a for α-Al_2O_3 (○), InGaAs (Δ), GaSb (◊) and W (●). The solid lines represent fits to slip distance theory using

Under the inhomogeneous loading of an indenter plastic strain is induced through movement of mobile dislocations through the crystal lattice. Each one of these dislocations can travel a mean free path (x) inducing a strain (ε_{pl}) limited by obstacles to dislocation motion such as grain boundaries, encountering free surface, sessile/immobile dislocations or plastic zone boundaries. The plastic strain in this case is

$$\varepsilon_{pl} = \rho_m b x$$

(Eq. 1.37)

where ρ_m is the mobile dislocation density and b is the effective Burger vector in the direction of slip. The mean free path (x) is taken to be proportional to the characteristic length scale (a) to give

$$x = a/\lambda$$

(Eq. 1.38)

where λ is a proportionality coefficient taken to be 1/3 as it is understood by continuum mechanics that the plastic zone encompasses a length of approximately 3a. The mobile

dislocation density is proportional to the total dislocation density with a proportionality coefficient $0 < \xi < 1$.

$$\rho_m = \xi\rho$$

(Eq. 1.39)

This gives a plastic strain

$$\varepsilon_{pl} = (\frac{\xi}{\lambda})\rho ba$$

(Eq. 1.40)

In the case of a single crystal, a dislocation within the plastic zone beneath an indentation must travel must travel past a pair of pinning points with a separation r, with a maximum length between points of 1/2πr. The pinning points have been taken to be other dislocations with an average spacing of $r = \frac{1}{\sqrt{\rho}}$. In order for a dislocation to overcome a pair of pinning points, there must be on average an elementary event for every r of dislocation line length for every distance r moved. The total line length of mobile dislocation within the strained volume is L. Any addition in the plastic strain will naturally lead to an increase in the mobile dislocation density and in the total line length of dislocations.

$$d\varepsilon_{pl} = xbd\rho_m$$

(Eq. 1.41)

$$dL = Vd\rho_m = a^3\rho_m = a^3\xi d\rho$$

(Eq. 1.42)

Accounting for the extra dislocations that have to move a distance (x) gives the number of necessary events to be

$$dN_{events} = \frac{dL}{r}\frac{x}{r} = \frac{\frac{1}{\lambda}ldL}{r^2} = \frac{\lambda a^2}{\xi b^2}\varepsilon_{pl}d\varepsilon_{pl}$$

(Eq. 1.43)

The flow stress given is

$$\tau = \tau_0 + \frac{dW}{d\varepsilon_{pl}} = \tau_0 + \alpha\left(\frac{\lambda}{\xi}\right)^{1/2}\mu\sqrt{b}\frac{\sqrt{\varepsilon_{pl}}}{\sqrt{a}}$$

(Eq. 1.44)

dW is the plastic energy per unit volume lost as heat. Relating the tensile flow stress by the shear flow stress with $\sigma = A\tau$ gives

$$\sigma = \sigma_0 + AC\mu\sqrt{b}\frac{\sqrt{\varepsilon_{pl}}}{\sqrt{a}}$$

(Eq. 1.45)

where A is the Taylor factor and C is the coefficient $C = \alpha(\lambda/\xi)^{1/2}$. Comparison of these expressions to those from indentation experimentation requires the use of the following relationship defined by Tabor as

$$P_m = 2.8\sigma$$

(Eq. 1.46)

The slip-distance model put forward here by Bushby et al confirms the experimental finding to give an indentation stress that scales with the inverse square root of the contact dimension (a) to give a relationship in the form

$$P_y = 2.8\left(\sigma_0 + AC\mu\sqrt{b}\frac{\sqrt{\varepsilon_y^{pl}}}{\sqrt{a}}\right)$$

(Eq. 1.47)

To investigate the influence of the material parameters ε_y^{pl}, b, P and P_0 equation 1.47 can be modified to give

$$\left(\frac{P_y - P_0}{P_0}\right)\frac{\sqrt{\varepsilon_y^{pl}}}{\sqrt{b}} = C\left(\frac{1}{\sqrt{a}}\right)$$

(Eq. 1.48)

Slip-distance theory has also been used to account for the interaction between the Hall-Petch (H-P) effect and the indentation size effect (ISE). The model builds upon previous work (Hou, Bushby, & Jennett, 2008) in which an empirical relationship was derived that enabled different sized indentations at the same strain for a given grain size to be plotted using the combined spatial frequency of all obstacles (D). This single length scale D is made up by combining the individual length scales of indentation size (a) and grain size (d) to give the relationship:

$$P_m = P_0 + \frac{K_{HP}}{\sqrt{D}} \quad \text{where} \quad \frac{K_{HP}^2}{D} = \frac{K_1}{a} + \frac{K_2}{d}$$

(Eq. 1.49)

where P_m is the mean indentation pressure or hardness (at constant strain), P_0 is the hardness of a single crystal, K_{HP} is a Hall-Petch like constant and k_1 and k_2 are scaling parameters. Again the plastic strain (ε_{pl}) follows the same relationship in regards to the mobile dislocations moving a mean free path (x);

$$\varepsilon_{pl} = \rho_m b x$$

(Eq. 1.37)

where ρ_m is the mobile dislocation density and b is the effective Burger vector. The increase in the stress on the mobile dislocations caused by mobile-sessile dislocation interactions is given by Taylor as:

$$\Delta\sigma = \alpha G b \sqrt{\rho_{TOTAL}}$$

(Eq. 1.50)

where G is the shear modulus, α is the Taylor coefficient, b is the Burgers vector and ρ_{TOTAL} is the total dislocation density. The Taylor coefficient α can be taken to be the scaling factor that defines the average spacing of dislocations to be equal to the mean free path between interacting dislocations which is equivalent to the inverse square root of sessile dislocation density. The change in stress on the mobile dislocation becomes

$$\Delta\sigma = G b \sqrt{\rho_s}$$

(Eq. 1.51)

$$\rho_s = \left(\frac{1-\lambda}{\lambda}\right) P_m$$

(Eq. 1.52)

where λ is a fraction of the total dislocation density ρ_{TOTAL}. Substituting equations 1 and 15 into equation 14 gives a modified Taylor equation;

$$\Delta\sigma(\varepsilon_{pl}) = G\sqrt{\left(\frac{1-\lambda}{\lambda}\right)}\frac{b.\varepsilon_{pl}}{x} \qquad \text{where } 0 \ll \lambda \ll 1$$

(Eq. 1.53)

Hou and Jennett (2012) suggest that this modified slip-distant model is in fact describing the combined length parameter D which they have define earlier (Hou, Bushby, & Jennett, 2008). There is no distinction between made between the individual length scales as the combination of them (D) is in fact defining the mean free path (x) described by slip-distance theory. In other words, all the characteristic length scales combine to constrain the mean free path of dislocations to form the components of plasticity. It has been shown that the ISE is actualised even when the contact radius (a) is approximately an order of magnitude greater than the grain size or dislocation cell network

dimension of a single crystal (a/l~10). Combining this with the work of Hou et al, 2008 gives a factor of 6x smaller to 10x larger for the indentation size relative to the grain size over which the ISE and SSE superimpose. This implies that the ISE and the SSE combine to drive the combined spatial frequency (D) as described by the slip-distance model to determine the indentation pressure P_m (Jennett, Hou, & Parlinska, 2012).

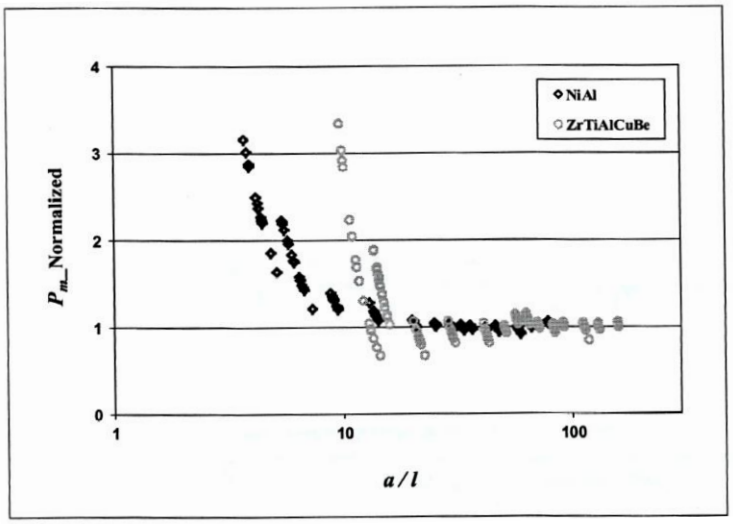

Figure 20: Indentation pressure normalised to the average indentation pressure at high indentation depths plotted against the ratio of contact size to structure size (Jennett, Hou, & Parlinska, 2012).

The authors were led to consider effects of other pinning points on dislocation motion and this is now introduced in the form of the average spatial frequency $\left(\sqrt{\rho_s}\right)$ where ρ_s is the line density of other pinning points. These pinning points can take the form of impurities, defects or voids, or pinned and pinning dislocations (Hou & Jennett, 2012). Equation 1.49 is modified to take the new form:

$$\frac{K_{HP}^2}{D} = \frac{K_1}{a} + \frac{K_2}{d} + K_{3\sqrt{\rho_s}}$$

(Eq. 154)

OR

$$P_m = P_y + \left(\frac{K_1}{a} + \frac{K_2}{d} + K_3\sqrt{\rho_s}\right)^{0.5}$$

(Eq. 1.55)

Where P_m is the mean indentation pressure, P_y is the indentation yield pressure for a dislocation of infinite extent to move in an infinite single crystal half space, K_1, K_2 and K_3 are scaling parameters with units GPa^2 μm and have a common factor:

$$G^2\left(\frac{1-\lambda}{\lambda}\right)\varepsilon_{pl}b$$

(Eq. 1.56)

The implication of which is that the $K_{1\text{-}3}$ values are dependent on the shear modulus (G), the Burgers vector (b), the coefficient λ and the plastic strain (ε_y^{pl}).

What are unclear are what the values of $K_{1\text{-}3}$ actually define, how they relate to the characteristic length scales and how they are influenced by the different pinning points. There is currently no experimental means of obtaining separate values for K_3 and $\sqrt{\rho_s}$ or differentiating between the pinning points that define the defect density. Hou et al have shown good agreement for Copper, what is now required is the application of the model to metals, ceramics and their composites to better test how the parameters influence the local stress-strain behaviour. However, it has been shown that the slip-distance model with a combined spatial frequency can be used to simulate the indentation pressure (P_m) when the contact radius is in an order of magnitude of the grain size.

1.10 Strain Gradient Plasticity

Strain gradient plasticity theory has also been used to explain size dependent behaviour using an internal length scale parameter. The model uses a strain gradient term to account for size dependence when the length scale associated with the deformation field is small compared to the material length scale. Plasticity causes dislocations to be generated, moved and to be stored. The storage and trapping of dislocations causes the material to work harden. Gradients of plastic

shear are attributed to the storage of geometrically stored dislocations (GND). Strain gradients exist due to geometry of loading or inhomogeneous plasticity. In the case of nanoindentation the level of plastic strain directly beneath the indenter is highest and zero when far enough from the surface. A theory of SGP based on the work of Fletch and Hutchinson is presented below. (Fleck , Muller, Ashby, & Hutchinson, 1994)

The relationship between the density of GNDs ρ_G and the local length scale λ is approximated to be

$$\rho_G \approx \frac{4\gamma}{b\lambda}$$

(Eq. 1.57)

where γ is the macroscopic plastic shear strain and b is the Burger's vector.

The GND contribution to the macroscopic shear yield strength τ is approximately

$$\tau \approx C'Gb\sqrt{\rho_G}$$

(Eq. 1.58)

Where G is the shear modulus and C' is a constant of order unity.

At smaller length scales, where the strain gradients are highest a greater number of dislocations are required. Therefore, there exists a regime where the number of GND is much higher than the SSD and it has been shown above that the hardness is dependent on the strain gradient, with the effect being more pronounced at smaller length scales.

To postulate a continuum theory of geometrically necessary dislocations the curvature tensor ζ is introduced and divided into its elastic and plastic components

$$\zeta = \zeta^{el} + \zeta^{pl}$$

$$\zeta_{ni}^{el} = e_{nkj}\epsilon_{ijk}^{el}$$

(Eq. 1.59)

$$\zeta_{ni}^{pl} = e_{nkj}\epsilon_{ijk}^{pl}$$

(Eq. 1.60)

The tensor ζ is used as an approximate measure of the density of GNDs. So the effective curvature tensor ζ_e with a magnitude direction is given as

$$\zeta_e = \sqrt{\frac{2}{3}\zeta_{ij}^{pl}\zeta_{ij}^{pl}}$$

(Eq. 1.61)

with the density of geometrically necessary dislocations taken to be

$$\rho_G = \frac{\zeta_e}{b}$$

(Eq. 1.62)

In a similar manner, the effective plastic strain ϵ_e is related to the plastic strain ϵ^{pl}

$$\epsilon_e = \sqrt{\frac{2}{3}\epsilon_{ij}^{pl}\epsilon_{ij}^{pl}}$$

(Eq. 1.63)

with the measure of statistically stored dislocations taken to be in stages 1 and 2 respectively

$$\rho_s = \frac{\epsilon_e}{\lambda_I b}$$

(Eq. 1.64)

$$\rho_s = \frac{\epsilon_e^2}{\lambda_u b}$$

(Eq. 1.65)

$\lambda_I + \lambda_u$ are fixed slip distances of the order $\lambda_I = 1\text{mm} + \lambda_G = 10\mu\text{m}$ and are thought to be correct to within one order of magnitude for other FCC metals.

Stages 1+2 represent mode of slip derived from the relationship between the density of SSD and GND as a function of shear strain γ for a range of microstructural length scales λ for pure copper. In stage 1, slip is confined to one system and dislocation storage is proportional to strain. Stage 2, slip is induced on secondary slip systems and the increase in dislocation storage leads to an increase in the critical resolved shear stress of slip modes according to Taylors relationship.

$$\tau_{CRSS} = \alpha b M \mu \sqrt{\rho}$$

A third stage exists where recovery mechanisms become active, such as climb, cross-slip and cell formations leading to a reduction in the dislocation density. (Cherkaoui & Capolungo, 2009)

With no distinction made between the elastic and plastic components of displacement and strain

$$\epsilon_e = \sqrt{\frac{2}{3}\epsilon_{ij}\epsilon_{ij}}$$

(Eq. 1.66)

$$\zeta_e = \sqrt{\frac{2}{3}\zeta_{ij}\zeta_{ij}}$$

(Eq. 1.67)

Using the Taylor equation $\tau = CGb\sqrt{\rho_s + \rho_G}$ as a basis, a relationship using a material length scale l with a single scalar strain measure φ is derived

$$\varphi^2 = \epsilon_e^2 + l^2\zeta_e^2$$

(Eq. 1.68)

Substituting equations 1.6, 1.8 and 1.9 into equation 1.2

$$\tau = CG\sqrt{\left(\frac{b\varepsilon_e}{\lambda_I}\right) + b\zeta_e}$$

For stage 1 (Eq. 1.69)

$$\tau = CG\sqrt{\left(\frac{b\epsilon_e^2}{\lambda_{II}}\right) + b\zeta_e}$$

For stage 2 (Eq. 1.70)

Using the harmonic mean $\frac{1}{2}\sqrt{\rho_s^2 + \rho_G^2}$ instead of the arithmetic mean $\frac{1}{2}(\rho_S + \rho_G)$ of the dislocation density gives

$$\tau = CG\left[\left(\frac{b\epsilon_e}{\lambda_I}\right)^2 + b^2\zeta_e^2\right]^{1/4}$$

(Eq. 1.71)

$$\tau = CG\left[\left(\frac{b\epsilon_e^2}{\lambda_{II}}\right)^2 + b^2\zeta_e^2\right]^{1/4}$$

(Eq. 1.72)

A model of strain gradient plasticity is presented using the Taylor model as the founding principles. This is because the Taylor hardening model is analogous to the Peach-Koehler force which is the stress required for a pair of interacting dislocations to pass one another. Likewise, the Taylor flow stress can be viewed as a *'passing stress'* for a mobile dislocation to move through a forest of dislocations without becoming pinned. Plasticity at micron and sub-micron length scales is described using the idea of statistically stored dislocations (SSD) and geometrically necessary dislocations (GND). GND are related to the plastic strain gradient and arise *because of the geometry of loading or inhomogeneous deformation in the material* (Gao, Huang, Nix, & Hutchinson, 1999). The model makes use of the internal material length parameter, l, which is thought to be related to the storage of GND.

Representing the contribution of the strain gradient in relation to internal length scale l and the smallest dimension of geometry D gives,

$$l\frac{d\varepsilon}{dx} \sim \varepsilon\left(\frac{l}{D}\right)$$

(Eq. 1.73)

This relationship helps to understand the transition between SGP theory which accounts for the "size effect" through strain gradients in nanoindentation experiments and conventional plasticity theories for macroscopic mechanical testing. As D becomes larger than parameter, l, the strain gradient contribution become negligible and when the parameters D and l are comparable, strain gradient effects dominate.

The basis for the Nix and Goa strain gradient plasticity model is Taylors relationship between shear strength and dislocation density

$$\tau = \alpha\mu b\sqrt{\rho_T} = \alpha\mu b\sqrt{\rho_s} + \rho_G$$

(Eq. 1.74)

Where ρ_T is the total dislocation density, ρ_s is the density of the statistically stored dislocations, ρ_G is the density of geometrically necessary dislocations, μ is the shear modulus, b is the Burgers vector and α is an empirical constant usually ranging from 0.2-0.5.

The effective strain gradient η can be defined as

$$\eta = \rho_G b$$

(Eq. 1.75)

Using the Von Mises yield criterion, the equivalent tensile flow stress can be expressed as

$$\sigma = \sqrt{3\tau} = \sqrt{3\alpha\mu b}\sqrt{\rho_{s+}\eta/b}$$

(Eq. 1.76)

In the absence of the strain gradient term, the uniaxial stress-strain law is

$$\sigma = \sqrt{3\tau} = \sqrt{3\alpha\mu b} + \sqrt{\rho_S} = \sigma_Y f(\varepsilon)$$

(Eq. 1.77)

Combining the above two occasions leads to a law for strain gradient plasticity

$$\sigma = \sigma_Y\sqrt{f^2(\varepsilon) + l\eta}$$

(Eq. 1.78)

where

$$l = 3\alpha^2 \left(\frac{\mu}{\sigma_Y}\right)^2 b$$

(Eq. 1.79)

The materials length scale, l, as introduced by Fleck and Hutchinson.

The materials length scale, l, is defined as the point at which the effects of strain gradient become comparable to those of strain. Significant strain gradient would equate to the point at which the density of SSD $\rho_s = 1/L_s^2$ and the density of GND $\rho_G = \eta/b$ are of the same order of magnitude.

$$\rho_s = \rho_G$$

$$\eta^{-1} = \frac{L_s^2}{b} = l$$

(Eq. 1.80)

"Therefore, the material length l is a fundamental length scale related to Burgers vector and dislocation spacing L_s at yielding, and is a fundamental measure of the deformation length at which geometrically necessary dislocations constitute a significant fraction of the total dislocation population." (Gao, Huang, Nix, & Hutchinson, 1999)

The material length l can be calculated from macroscopically measurable material properties.

$$l = 3\alpha^2(\mu/\sigma_Y)^2 b$$

(Eq. 1.81)

There arises a conflict from using the Taylor model as a basis for SGP in that a large cell size containing enough dislocations is needed to accurately calculate the flow stress. However, a small cell size is required to accurately calculate the strain gradient. A new parameter is introduced to resolve the conflict in calculating the strain gradient and flow stress accurately. A suitable definition for the cell size l_ε is given as

$$l_\varepsilon = \beta L_{yield} = \beta \frac{\mu b}{\sigma_Y}$$

(Eq. 1.82)

Where L_{yield} is the mean spacing between statistically stored dislocations at yielding and $\beta < 1$ is a constant coefficient to be determined to be determined from experiments $\beta = 1 - 10$ ensures that the mean spacing between SSD is always smaller than that of the cell size l_ε.

Both the Fleck and Hutchinson (FH) and the Nix and Goa (NG) models share some similarities but are also quite different in their founding principles and results when fitting to the mechanical data results. The FH model considers contributions to flow stress on both the SSD and GND whereas the NG model only considers the contribution of the density of GND. A limitation of the NG and FH models is that neither considers the interaction between GND and SSD. Both models also employ isotropic measure of the plastic strain and its gradient. A modified J_2 theory of plasticity is used when the size dependence becomes important when the strain gradient is large compared to the length scale. What is also apparent is that the strain gradient increases the rate of strain hardening for the NG model and the yield strength for the FH model with an under prediction of strain hardening measurements found experimentally. (Evans & Hutchinson, 2009) Subsequently both models give very different length scales for the same experimental parameters. There has been an effort to expand on the models (Niordson & Hutchinson, 2011) through the addition of new parameters to better fit the data, but there remains much confusion

and ambiguity around the original model and its fundamentals in nanomechanics. (Liu & Dunstan, 2017)

1.11 Micro-pillar Compression

Micro-pillar compression experimentation first gained notoriety following the test methodology developed by Uchic et al, 2002 in which cylindrical pillars were milled into a bulk crystal surface using a Focused Ion Beam (FIB). Micro-pillars of diameters ranging from ~100nm to 40µm have been fabricated using this method and uniaxial compression tests carried out with flat punch tips using traditional nanoindentation systems. Although the systems are typically used for depth-sensing indentation experiments their ability to produce good stress-strain resolution at low loads and depths make them ideal for micro-compression testing. Bulk Nickel single-crystals were chosen to be the model for the Uchic et al methodology, due to its well-known mechanical properties. Single-crystal also allows for fabrication of grain boundary free structures in which the only barriers for dislocations are the free surfaces.

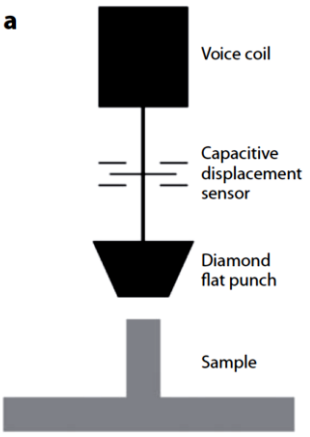

Figure 21: Schematic diagram of the Uchic et al micro-compression test (Uchic et al, 2009)

The stress-strain curve data for compression of defect free pillars shows a strong flow stress dependence on the sample size, where the flow stress is observed to increase with the reduction in the diameter of the pillars (Uchic et al, 2002, 2004, 2009)(Greer et al, 2005 & 2008) (Greer & Nix , 2006) (Frick et al, 2008).

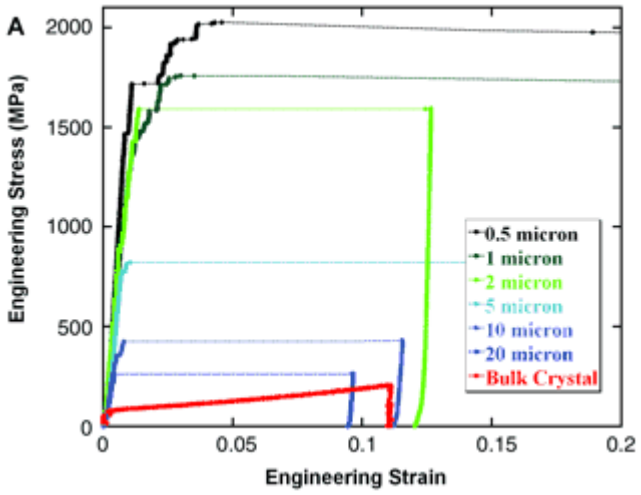

Figure 22: Stress-strain curves for micro-pillars ranging in size from 20 to 0.5µm in diameter, as compared to the behaviour of a bulk single crystal. (Uchic et al, 2004)

The deformation behaviour of pillars demonstrates some unique mechanisms at work, in as much as there is characteristic stochastic strain bursts or discontinuous yield behaviour. This differs from the smooth conventional elastic-plastic transition of bulk materials that are associated with constant work hardening. Analysis of the loading curves shows that shows that there is some plastic activity preceding the random strain bursts which in itself is separated by elastic loading, described as a self-organising process (Uchic et al, 2004). The almost random and rapid flow can be attributed to some catastrophic event that has the ability to nucleate and propagate dislocations within the structures. Dislocation sources are exhausted faster than they can be nucleated in the smallest of volumes and therefore lead to a starved state or exhaustion-type hardening (Schneider, et al., 2013). Perhaps the best experimental evidence of the dislocation starvation model exists in the work of Ng & Ngan, 2009 in which Aluminium micro-pillars are coated or centre-filled with tungsten to trap the dislocations by preventing annihilation at the free surface. The data from compression testing reveals smoother curves with higher rates of strain hardening for coated pillars over non-coated pillars. This behaviour can be attributed to the dislocation trapping effect of the tungsten coating which allows for high density dislocation storage in newly formed dislocation cell networks as observed by TEM observations (Shan et al, 2008) and by consequence suppressing nucleation controlled plasticity (Greer et al, 2011).

This could also explain the softening behaviour attributed to pre-strained crystals, as the energy required to initiate plastic flow is greater if a dislocation nucleation process is required rather than if a dislocation source already exists. The effect of bulk pre-straining can be categorised into two regimes, a sub-micron and a bulk/micron regime (Fig. 23). In the case of the bulk regime the strain hardening rate can be attributed to dislocation-dislocation interactions or a Taylor-type hardening within the dislocation cell walls giving a strain rate dependence on dislocation density. Whereas for the sub-micron regime there is unlikely to exist a complete cell structure within which dislocation motion is hindered meaning that the nearest obstacle is in fact the free surface. This reduced mean free path reduces the initial flow stress and thus leading to a starved or exhausted state with increased strain. Bei et al, 2008 have also shown that pre-straining leads to softening behaviour of Molybdenum micro-pillars. The as-grown pillars behaved like dislocation free materials in that the yield strength approached the theoretical strength, pre-strained pillars of 11% showed strength comparable to bulk even into the sub-micron regime demonstrating no size dependence.

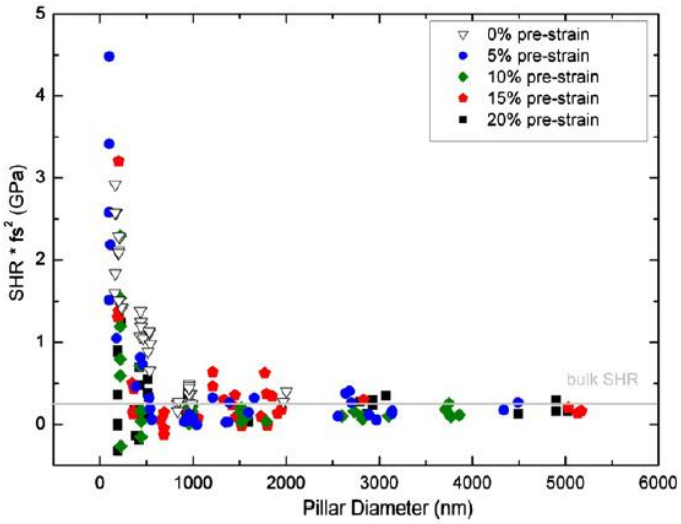

Figure 23: Strain hardening rate (SHR) versus pillar diameter for pre-straining values of 5%, 10%, 15% and 20% (Schneider, et al., 2013)

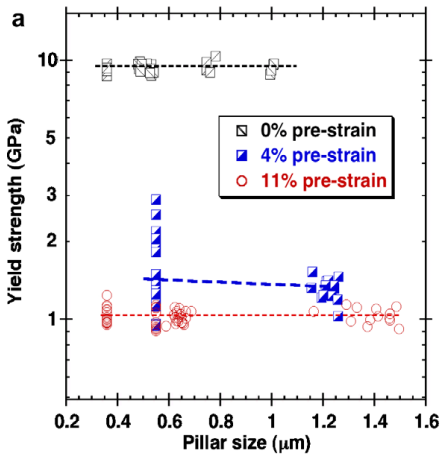

Figure 24: Dependence of yield strength on pillar size for different pre-strains (Bei et al, 2008)

2. Nanoindentation background and Principles

2.1 Load-Displacement Curves

Indentation testing can be used to derive important mechanical properties of materials in a non-destructive test for sub-micron or nano sized specimens. This is possible due to the development of sensitive force and displacement measuring instruments with automated technologies. The mechanical properties that can be derived directly through load-displacement curves are the elastic modulus, the hardness, yield behaviour and plastic deformation, all of which form the fundamentals of materials behaviour in ceramics and metals. There are currently two widely used methods of implementing and analysing load-displacement curves, the Oliver and Pharr Method and the Field and Swain method. Both are summarised below.

2.2 Field and Swain Method

This methodology of analysing load-displacement data to derive the elastic modulus and hardness of a material works by a loading-partial unloading technique. At each force increment the load is reduced to some value below the maximum, typically 75% to allow for elastic recovery, and force equilibrium is assumed at each stage before continuing to a new higher load. This allows for separation of the elastic and plastic components and therefore the hardness and the elastic modulus can be defined as a function of depth (Field & Swain, 1993). This technique works only for a spherical indenter with the condition that the radius of the indenter contact must be less than the radius of the spherical indenter.

Using Hertz's contact mechanics, Johnson (1985) has shown that the penetration (h_e) of sphere of radius (R) into the surface under a force (F) is expressed as

$$h_e = \left(\frac{9}{16}\right)^{1/3} \left(\frac{F}{E^*}\right)^{2/3} \left(\frac{1}{R}\right)^{1/3}$$

(Eq. 2.1)

E^* represents the composite modulus of the contact between the surface and the indenter which are considered to be elastic bodies that deform under a force (F). The composite modulus is given by (Field & Swain, 1993)

$$\frac{1}{E^*} = \frac{(1 - v_s^2)}{E_s} + \frac{\left(1 - v_i^2\right)}{E_i}$$

(Eq. 2.2)

where E is the Young's modulus, v is the Poisson's ratio and the subscripts s and i refer to the surface and indenter respectively. The initial response of the surface upon loading is entirely elastic, the depth of penetration in contact with the sphere (h_c) is less than the total depth (h_{max}) and follows the ratio

$$h_c = \frac{h_{max}}{2}$$

(Eq. 2.3)

The radius of contact between the surface and the sphere over which the force is applied (indentation pressure) is

$$a^2 = Rh_e$$

(Eq. 2.4)

R is a function of h_c and requires a calibration to determine the indenter radius at any given depth. This is due to the fact that the indenters are not of ideal spherical geometry and exhibit blunting at the tip.

Upon unloading of the force in an elastic-plastic scenario the material recovers elastically from the maximum depth (h_{max}) to leave a residual depth (h_r) of plastic deformation. The elastic recovery is expressed as

$$h_e = h_{max} - h_r$$

(Eq. 2.5)

Since the total elastic component $h_c = h_{max} - h_r$, half of which lies above the circle of contact , the plastic component is (Field & Swain, 1993)

$$h_c = \frac{h_{max} + h_r}{2}$$

(Eq. 2.6)

The radius of the circle of contact (a) is therefore (Field & Swain, 1993)

$$a^2 = 2Rh_c - h_c^2$$

(Eq. 2.7)

The unloading region requires a different form of analysis as it only contains elastic recovery whereas the loading region transgresses from elastic to plastic. The reloading involves deformation of the exiting residual impression formed during the initial loading process which has a radius of curvature R', larger than the indenter radius due to the elastic recovery of the material. Equation 2.1 becomes

$$h_e = \left(\frac{9}{16}\right)^{1/3} \left(\frac{F}{E^*}\right)^{2/3} \left(\frac{1}{R} - \frac{1}{R'}\right)^{1/3}$$

(Eq. 2.8)

where $[(1/R) - (1 - R')]$ is the relative radius of curvature between the sphere and residual impression respectively (Bushby, 2001) (Fischer-Cripps, 2002). It is assumed that elastic recovery of the residual impression happens only in the vertical direction to give a radius of curvature of

$$R' = \frac{a^2 + h_r^2}{2h_r}$$

(Eq. 2.9)

The elastic modulus can now be calculated from the unloading curve with the expression

$$E^* = \frac{3}{4}\frac{F}{h_e^{3/2}}\left(\frac{1}{R} - \frac{1}{R'}\right)^{1/2}$$

(Eq. 2.10)

The depth of a residual impression can be calculated by measuring the load and displacements for each data pair to give a ratio of the elastic displacements

$$h_r = \left[\frac{h_2(F_1/F_2)^{2/3} - h_1}{(F_1/F_2)^{2/3} - 1}\right]$$

(Eq. 2.11)

where F is the load measured from the data points and h is the displacements/penetration. The subscripts 1 and 2 denote the one part of the data pair, from the loading and unloading curve respectively.

2.3 Oliver and Pharr Method

This method builds on the work of Sneddon in the 1960s in which he derived solutions for punches of a conical and parabolic nature under elastic loading conditions. The behaviour of a Berkovich indenter is shown to be described by that of parabolic indenter because the point of plasticity can't be sufficiently defined and the pressure distribution which forms around the tip is more like that predicted by a parabola. This is understandable as no tip is perfectly sharp but more rounded, due to the limitations in manufacturing an ideal tip (Oliver & Pharr, 1992). This method can be applied for use with a spherical indenter or any indenter with a geometry that can be described as a solid of revolution of a smooth function. This method is also independent of indenter geometry which means it is still relevant when the contact area changes upon unloading (Pharr, Oliver, & Brotzen, 1992b). The method for spherical indentation is demonstrated (Fischer-Cripps, 2002).

The Oliver and Pharr method uses the experimentally measured stiffness ($S = \frac{dP}{dh}$) of the upper portion of the unloading data to determine the depth of penetration in contact with the sphere (h_c). The slope for the elastic unloading without reverse plasticity is the derivative of the equation given by Hertz to describe the elastic recovery (h_e) as a function of load (P).

$$P = \frac{4}{3} E^* R^{1/2} h_e^{3/2}$$

$$\frac{dP}{dh} = 2E^* R^{1/2} h_e^{1/2}$$

(Eq. 2.12 and Eq. 2.13)

Substituting equation 2.13 into 2.12 gives

$$P = \frac{2}{3} \frac{dP}{dh} h_e$$

(Eq. 2.14)

Rearrange to give

$$h_e = \frac{3}{2} P \frac{dh}{dP}$$

(Eq. 2.15)

Upon unloading the circle of contact beneath the free surface is half the elastic displacement $h_a = h_e/2$. At maximum load h_a is given as

$$h_a = \left[\frac{3}{4}\right] \frac{P_t}{dP/dh}$$

(Eq. 2.16)

The following relationship is known

$$h_{max} = h_c + h_a$$

$$h_c = h_{max} + \frac{h_e}{2}$$

(Eq. 2.17)

The contact radius can now be calculated

$$a = \sqrt{2R_i h_p - h_p^2}$$

(Eq. 2.18)

The composite modulus can be calculated using the initial part of the unloading curve

$$E^* = \frac{dP}{dh}\frac{1}{2a}$$

$$E^* = \frac{\sqrt{\pi}}{2}\frac{S = (\frac{dP}{dh})}{\sqrt{A}}$$

(Eq. 2.19)

where A=πa^2, the area of contact (Field & Swain, 1993) (Fischer-Cripps, 2002).

2.4 Spherical Indenter Area Function

Knowing the precise geometry of a spherical indenter is vital to accurately determining the elastic and plastic properties of a material using contact mechanics. However, the case is that indenter tips deviate from perfect spherical geometry because of the difficulty in trying to polish

an anisotropic crystal into a spherical shape at such small length scales. It is because of this irregularity in the indenter shape that we have the greatest uncertainty in indentation measurement especially at the smallest length scales, for which small loads are important (Ma & Levie, 2007). The departure of the indenter tip from ideal geometry is represented by the area function, which gives the contact area as a function of the contact depth and is derived from experiments on reference materials with a wide range of known elastic moduli (Fischer-Cripps, 2010). A method for determining the area function given by Bushby and Jennett, 2001 is explained below.

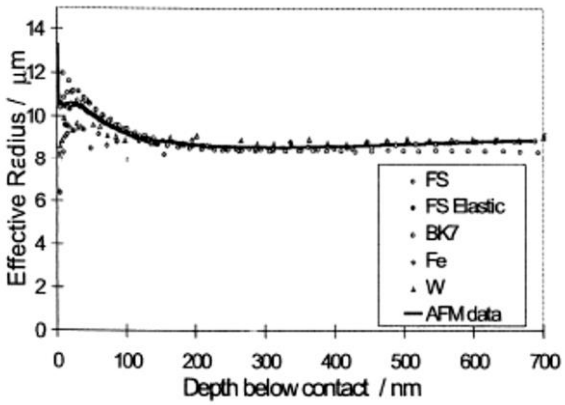

Figure 25: Effective indenter radius (R_{eff}) against the depth in contact with the indenter surface (h_c) for an elastic-plastic indentation for a range of reference materials. Nominal radius of spherical indenter 10µm with a frame compliance of 0.24nm/mN (Bushby & Jennett, 2001).

From Hertzian contact mechanics the elastic displacement (h_e) from an elastic contact between an elliptical body and a planar surface is given by Johnson, 1985 as

$$h_e = \left(\frac{9}{16}\right)^{1/3} \left(\frac{F}{E^*}\right)^{2/3} \left(\frac{1}{R}\right)^{1/3}$$

(Eq. 2.20)

where F is the applied force, R is the radius of the sphere and E^* is the composite modulus of the elliptical body in this case the sphere and the surface. The composite modulus is given by

$$\frac{1}{E^*} = \frac{(1 - v_s^2)}{E_s} + \frac{\left(1 - v_i^2\right)}{E_i}$$

(Eq. 2.21)

where E is the Young's modulus, v is the Poisson's ratio and the subscripts s and i refer to the surface and indenter respectively. What is actually measured during experimentation to calculate the effective radius of the indenter is

$$h_e = h_m + h_0 - C_f F = \left(\frac{9}{16}\right)^{1/3} \left(\frac{F}{E^*}\right)^{2/3} \left(\frac{1}{R_{eff}}\right)^{1/3}$$

(Eq. 2.22)

where h_m is the measured penetration, h_0 is the penetration revised using the initial contact depth made at first contact with the surface, C_f is the instrument frame compliance, R_{eff} is the effective indenter radius or area function (Bushby & Jennett, 2001). The values for the instrument frame compliance (C_f), the composite modulus (E^*) and the effective indenter radius (R_{eff}) can be confirmed by indenting in to a group of materials with a wide range of elastic moduli, most commonly Fused Silica, Tungsten and soft metals such as Iron. The most preferential materials being homogeneous and isotropic in nature with a flat surface free of imperfections. Successful superposition of the data on an effective radius versus depth below contact plot validates the input parameters. The range of calibration for the area function of a indenter tip with a radius, R<10µm is limited by the depth at which the elastic regime exists, therefore equation 32 must be modified to accommodate the elastic-plastic regime.

$$h_e = \left(\frac{9}{16}\right)^{1/3} \left(\frac{F}{E^*}\right)^{2/3} \left(\frac{1}{R} - \frac{1}{R'}\right)^{1/3}$$

(Eq. 2.23)

where $[(1/R) - (1 - R')]$ is the relative radius of curvature between the sphere and residual impression respectively. It is assumed that elastic recovery of the residual impression (h_r) happens only in the vertical direction to give a radius of curvature of

$$R' = \frac{a^2 + h_r^2}{2h_r}$$

(Eq. 2.24)

And a radius of the circle of contact (a)

$$a^2 = 2Rh_c - h_c^2$$

(Eq. 2.25)

The depth of the residual impression (h_r) that would be left after fully unloading from a load F_1 is given by

$$h_r = \frac{h_1 - (F_1/F_2)^{2/3} h_2}{1 - (F_1/F_2)^{2/3}}$$

(Eq. 2.26)

where F is the load, h is the penetration below the surface and the subscripts 1 and 2 refer to the pair of load and unload data respectively. The surface depth in contact (h_c) with a non ideal spherical indenter is expressed as

$$h_c = \frac{h_1 + h_2}{2}$$

(Eq. 2.27)

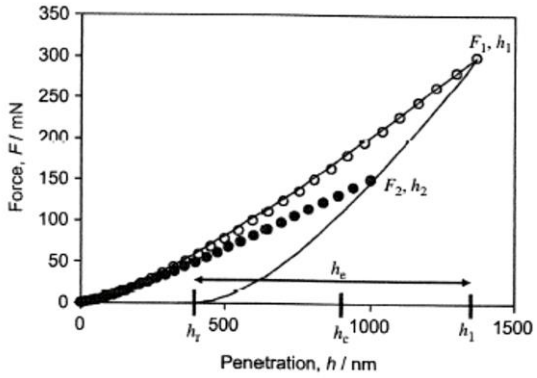

Figure 26: An example of force-penetration data using the partial unloading method of Field and Swain. The solid line shows the load- full unload curve for a set of data points F_1, h_1 and F_2, h_2 resulting in an elastic displacement (h_e) with a residual impression (h_r).

The application of these equations in determining the depth of contact between the surface and the indenters assumes that the radius of the indenter is the same at the loading and loading change sue to the fact that the fraction unload is small only 25% in this case. This is not considered significant enough to have an impact on the data as the indenter radius does not change by any more than a factor of 2 for the whole range of indentation. It is also safe to assume that there will be no lateral shrinkage of the indented surface upon unloading (Zhu, Hou, Bushby, & Dunstan, 2008b).

Using Hertzian contact mechanics, the non-ideal indenter radius can be calculated by substituting equations 2.24 and 2.26 into equation 2.25 and solving for R, this gives

$$(2Qh_c^2)R^2 + (2h_r - 2h_c + Qh_r^2 - Qh_c^2)R + (h_c^2 + h_r^2) = 0$$

(Eq. 2.28)

where $Q = (\frac{16}{9})(\frac{E^{*2}}{F^2})h_e^3$. The positive root of equation 2.28 being the effective radius for a given depth below contact.

There are many conditions to consider that may contribute to uncertainties in measurements during indentation testing. The effective radius of the indenter (R_{eff}) is particularly sensitive to force and depth measurements as it follows a $R \propto 1/h^3$ relationship. At low contact depths (h_c) the data becomes increasing susceptible to the effects of surface conditions in which there is a deviation from theoretical elastic behaviour (effect on E^*) and there begins an interaction between two non-zero roughness surfaces. For higher contact depths, the effective indenter radius becomes particularly sensitive to the frame compliance (C_f) and unreliable for ductile metals due to effect of pile-up and sink-in and for ceramics because of cracking events (Bushby & Jennett, 2001) (Zhu, Hou, Bushby, & Dunstan, 2008b). Again, superposition of the data for a range of elastic moduli is required to ensure all input parameters are correct as there many unknowns in the determination of the effective indenter radius.

The validation of the area function for an indenter continues with direct measurement of the indenter tip using atomic force microscopy (AFM). The AFM tip is calibrated and yields a maximum uncertainty in the measurements of 9-20nm with a minimum scan size of ≈3.9µm used to maximise pixel resolution. Validity of the images is confirmed by reproducing the images using different scan directions and sample positions and implies there is little effect of thermal or mechanical drift. A similar method for determining the area function using metrological scanning force microscopy (SFM) is used by Herrmann et al, 2000 for ball shaped indenters. The measured indenter radius is seen to increase rapidly with increasing indentation depth with a drop in the relative standard deviation of the indenter radius as the distance increases from the indenter tip. Comparison of the area function determined through indentation testing and AFM measurement yields a difference in the R_{eff} vs. h relationship in which a translation of at least 2nm is required for superimposing the data. The difference is born through the manner of measurement in which the AFM dimensions in the Z plane scan at the most extreme features of the indenter tip and this measurement is combined with contributions from surface roughness,

vibration and noise. Whereas what in fact is measured through indentation measurements is the response of the material without any impact by surface layer effects, this response can be taken to be more reliable in calculating the effective radius of the spherical tip as the depth in contact with the tip can be derived straight from the response of the material. This demonstrates the validity of the Hertz equation in determining the effective radius function for both elastic and elastic-plastic indentation responses.

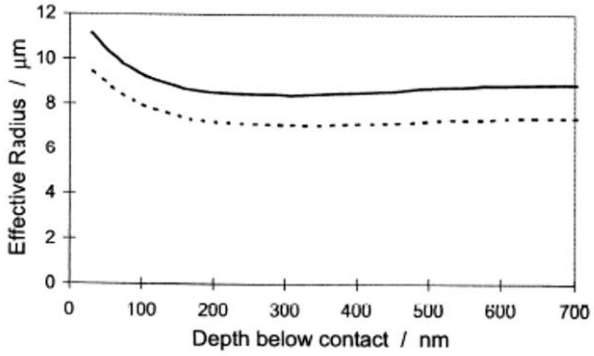

Figure 27: Difference in the depth calibration using Hertzian contact mechanics on the force-penetration data and AFM results in a vertical translation of the R_{eff} vs h data.

3. Microscopy Mapping and Imaging techniques

3.1 Transmission Kikuchi Diffraction (TKD)

Transmission Kikuchi Diffraction (TKD) differs from Electron Back-Scattered Diffraction (EBSD) in that the specimen is mounted perpendicular to the conventional EBSD mounting position of/at -20 degrees, resulting in the reduction in the intensity of back scattered electrons detected and an increase in the intensity of the electrons forward scattered in transmission. A significant advantage of TKD over EBSD is that a spatial resolution as small as 2nm-10nm can be achieved (Trimby, et al., 2014). Typical working conditions reported for TKD have some degrees of variation, with working distances in the range of 3-12mm, accelerating voltages between 20kV and 30kV and beam current as low as 400pA and as high as 10nA being used(Trimby, et al., 2014) (Keller & Geiss, 2012) (Trimby P. W., 2012).

Kikuchi diffraction patterns are generated by the interaction of the primary electrons with the specimen surface. The primary electrons are scattered elastically and in-elastically through the specimen as they interact with the matter, some of which will satisfy the Bragg angle of diffraction for the lattice planes. The diffracted electrons are detected as they strike the Phosphor screen to produce what is known as Kikuchi lines/patterns.

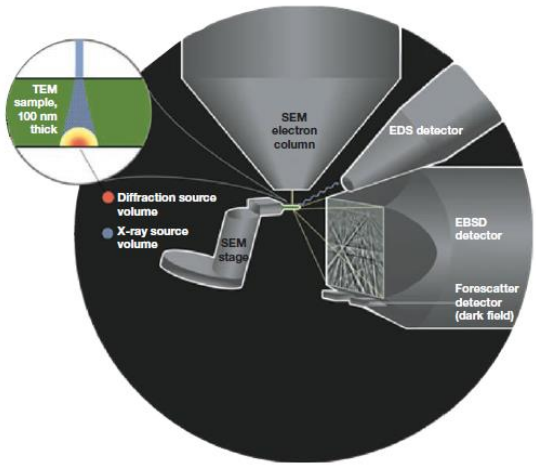

Figure 28: Schematic illustration of the TKD setup inside the SEM chamber (Trimby & Cairney, 2014)

Monte Carlo scattering simulations can explain the concept behind improved spatial resolution of the TKD technique over EBSD. The distribution of scattered electrons at the point of exit from the surface is significantly smaller (8nm-16nm) for electron transmission, whereas in the case of back-scattering the distribution of electrons can be in the region of 70nm (Keller & Geiss, 2012). This results in a condensed volume of interaction which allows spatial resolutions of 10nm to be realistically achieved thus, enabling the mapping of significantly smaller structures than was previously possible using the conventional EBSD system. Perhaps the most significant benefit is that the reduced pattern source volume allows for good diffraction pattern collection from areas of high dislocation densities. The simulations of electron scattering events also reveal that coinciding with the decline in the electron scattering distribution there is also narrowing of the electron energy distribution. Both outcomes suggest that there are considerably less scattering events occurring in transmission which contributes to the overall effectiveness of the TKD technique as means of analysis (Keller & Geiss, 2012).

Tilting of the sample 70 degrees in the direction of the Phosphor screen as done in the EBSD setup improves the signal from the back-scattered electrons, but contributes to the increase in scattering of electrons and the spatial resolution perpendicular to the tilt axis(Brodusch, Demers, & Gauvin, 2013). This gives rise to an inferior spatial resolution versus TKD, in some cases being an order of magnitude higher.

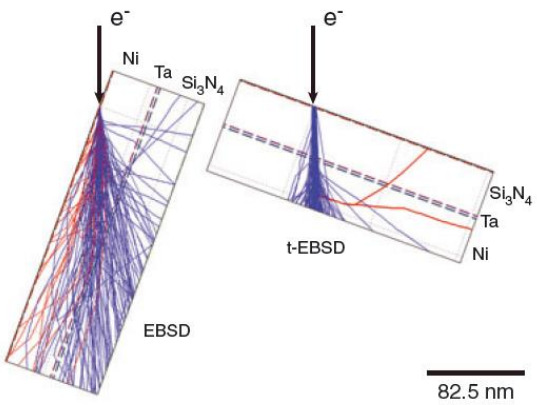

Figure 29: Monte Carlo Simulations of scattering events in 40nm-Ni/ 2.5nm-Ta/ 40nm-Si_3N_4 Amorphous. 38 keV accelerating voltage. Red trajectories indicate back scattering events and blue trajectories indicate electron transmission. (Geisse, Rice, & Keller, 2013)

Work by Rice et al, 2014 demonstrated the region from which the Kikuchi Diffraction Patterns (KDP) are detected by comparing two polycrystalline Au and amorphous Si_3N_4 bilayer films. Specimen 1 is composed of 10nm poly-Au/20nm a-Si_3N_4 and specimen 2 is composed of 10nm poly-Au/50nm a-Si_3N_4. Having the specimens arranged with the Au film 'face up' there was *"diffuse, but recognisable, patterns"* and *"no patterns* "observed for each specimen respectively. However, having the specimens arranged with the Au film 'face down' patterns were *"readily seen for both specimens"* showing *"more contrast and greater pattern sharpness"*(Rice, Keller, & Stoykovich, 2014). It can be concluded from these bilayer film experiments that the scattering events that produce the observable Kikuchi diffraction patterns occur near the free surface from which the transmitted electrons escape. The electrons contributing to the TKDP can be characterised as higher energy in-elastically transmitted electrons(Rice, Keller, & Stoykovich, 2014).

Energy losses in transmission due to scattering can occur throughout the thickness of the film. It is highly unlikely that the electrons scattered at shallower depths contribute to the diffraction pattern as they are scattered further before escaping or may undergo addition scattering events before exiting the free surface. Increased scattering associated with thicker specimen thickness will cause an expansion in the TKD pattern source volume and therefore a loss in spatial

resolution or in the case of fine grained materials overlapping of patterns from adjacent grains (Trimby P. W., 2012).High energy electrons have undergone little scattering and have therefore been transmitted via the most direct route through the film contributing to very little beam broadening. Considering the above observations, it is therefore of great significance to ponder upon the effect of the film thickness on beam broadening in relation to the spatial resolution for structure mapping.

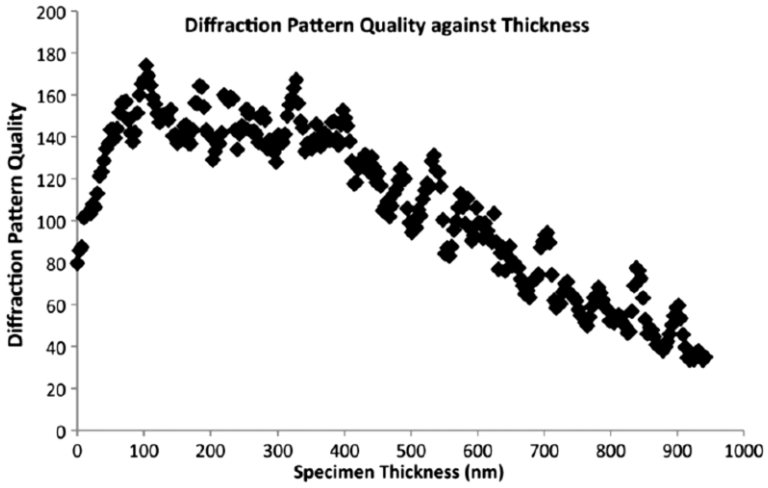

Figure 30: Sample thickness against diffraction pattern quality measured as a function of Kikuchi band contrast for Al-Alloy with 22kV accelerating voltage (Trimby P. W., 2012)

A clear relationship between the specimen thickness and the diffraction pattern can be seen in figure 3.1. Good pattern quality can be acquired from samples with thicknesses between 75nm and 400nm with an accelerating voltage of 22kValthough, for most materials thickness of less than 100nm is optimal (Trimby & Cairney, 2014). Varying the accelerating voltage of the electron beam depending on the thickness of the specimen is also known to improve KDP quality. Optimum specimen thicknesses for the highest quality KDP were found to be in the range of 75nm to 200nm (Trimby P. W., 2012), although conditions such as the primary beam conditions and the specimen density all contribute to the KDP quality.

3.2 Electron Channelling Contrast Imaging (ECCI)

Electron channelling contrast imaging is a scanning electron microscope technique that is utilised to image near surface crystal defects in tilted electron opaque samples using the detected back scattered signal.

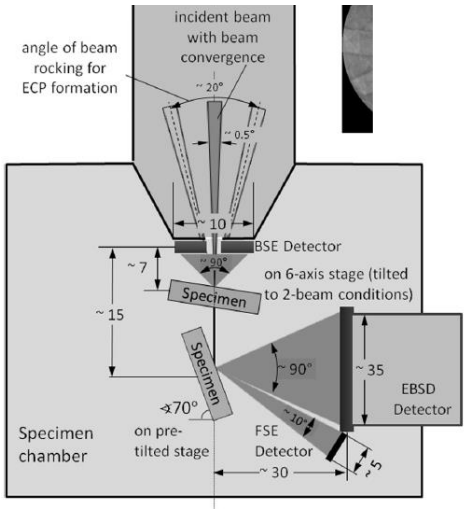

Figure 31: Schematic diagram of an ECCI and EBSD set up (Zaefferer & Elhami, 2014)

The electron backscattering intensity obtained from a crystal is highly dependent upon the incidence direction of the primary electron beam relative to the crystal lattice planes and not necessarily dependent on the normal sample surface (Simkin & Crimp, 1999). This condition is known as the Bragg angle and defines the intensity of the back scattered electrons. Meeting the condition where the incidence electron beam and the crystal lattice planes are equal $\theta_E = \theta_B$ produces very little back scattering of electrons (Zaefferer, Elhami, & Gutierrez, 2011). This makes the ECCI technique very sensitive to lattice orientation because the difference between fulfilling and not fulfilling the Bragg condition is in the order of less than $1°$. (Barnoush, 2012) .

ECC is very effective for imaging crystal defects such as dislocations, cracks and grain boundaries, as well as elastic and plastic strain fields (Kaboli, Goldbaum, Chromik, & Gauvin, 2013). This is because electron channelling contrast is achieved through the difference in crystal orientation

caused by the defects or deformation. The generation and propagation of dislocations through plastic deformation distorts the crystal lattice locally and this allows a contrast to be found between to the two regions. In the case of heavily deformed regions there may be various changes in satisfying the Bragg angle condition causing the visible aspects of the deformation zone to change with the angle of tilt (Welsch, Henning, Marx, & Vehoff, 2007).

The electron wave fulfilling the Bragg condition for a set of crystal lattice planes is elastically and coherently scattered producing a low backscatter intensity signal. However, the BSE energy signal consists of electrons with a broad energy distribution, electrons interacting with matter experience a range of scattering phenomena;

Phonon Scattering or thermal diffuse scattering (TDS): The most common inelastic scattering event detected in the backscattered signal. Whereby the high-energy electrons from the primary beam interact with the electrons in the specimen causing a transfer of energy (>1eV). This transfer of energy generates lattice oscillations (phonons) as the atoms are bonded together elastically, which in turn generates heat that is propagating locally through thermal conductivity. Thermal diffuse scattering is a by-product of the increase in temperature caused by phonon generation. An increase in temperature increases the magnitude of the lattice oscillations and in so doing increases phonon scattering. (Williams & Carter, 2009)

Secondary Electrons: Electrons emitted from the material by the beam electrons through a transfer of energy allowing promotion of electrons from the conduction and valence bands. The kinetic energy of the secondary electrons is sufficient for propagation through the material and will be subject to inelastic scattering events. The secondary electron can only escape the specimen surface if it has sufficient energy to overcome the surface energy barrier.

Bremsstrahlung X-rays: Primary electrons interact with the Coulombic field of the atomic nucleus and experience deceleration i.e. a change in momentum. The energy lost by the incident

electron generates electromagnetic radiation (X-rays) with the energy of the X-rays equal to the loss in energy of the incident electron. The energy loss is dependent on the interaction with Coulombic field, the X-rays can have energies up to the beam energy.

Auger Electrons: High energy incident electrons can eject an inner shell atomic electron leaving vacancies which are subsequently filled by higher energy electrons. The loss in energy which is the difference between the original excitation energy and the binding energy of the outer shell is transferred to an electron. This change in energy is transferred to a higher orbital electron which is emitted as an Auger electron. (Goldstein, et al., 1992)

The ECCI technique allows for a probing depth of approximately 50nm-100nm below the surface depending on conditions and cannot be used exclusively to understand the three-dimensional structure of the plastic zone. ECCI is also limited in that no useful information can be extracted from the area directly below the indent due to the surface curvature and the high dislocations density within the hemispherical core producing high levels of lattice rotations (Zhang, Zaefferer, & Raabe, 2015).

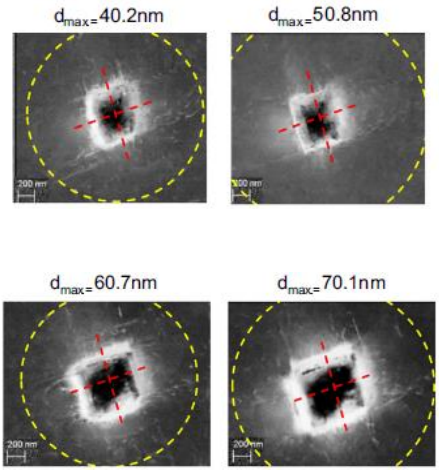

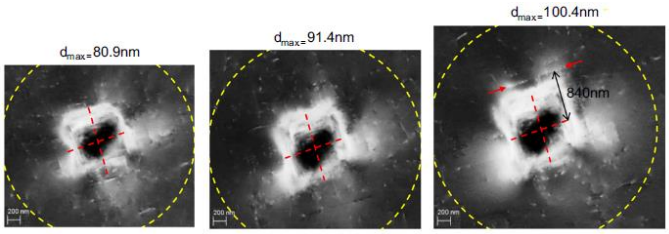

Figure 32: ECC images of the dislocation structure around nano-indents of depths between 40nm-100nm (Zhang, Zaefferer, & Raabe, 2015).

Due to the highly-localised lattice distortions of high dislocation density areas in and around an indentation, the effective area being imagined will change according to where the Bragg angle condition is being met. Therefore, tilting through a range of angles will allow for different dislocation structures to be observed, ECCI is disadvantaged in that the entire deformation zone cannot be imagined at once. This can be overcome by superimposing images on each other from a range of angles (Barnoush, 2012). Where individual dislocations can be clearly distinguished in images, the dislocation density can be estimated using the relationship

$$\rho = \frac{2N}{Lt}$$

Eq. 3.1

Where N is the number of dislocation line intersecting a grid of total line length L and t is the probe length (Gutierrez-Urrutia & Raabe, 2012).

4. Micro-Pillar Indentation of Pre-Strained Nickel Single Crystal

4.1 Experimental Details

Understanding the mechanical response of the Nickel single crystal is a prerequisite to introducing a variable such as the free surface around the pillar edge. Pillar diameters at integers of contact size can only be produced if the contact size is known at predetermined strain levels on bulk tests. Surface preparation for indentation was carried out using mechanical polishing, beginning with coarse silicon carbide polishing disks and proceeding to finer silicon carbide polishing disks. The final surface finish was achieved using electro polishing to achieve a sub-micron finish of ≈30nm.

An UMIS 2000 was used with 3.5µm and 5.0µm spherical tips to extrapolate the indentation stress-strain curves. Contact sizes at a/R=0.1 and a/R=0.35 were chosen as particularly significant as strain at these values occur just after the point of yield and after significant plasticity respectively. The contact sizes at these strain levels was recorded by taking an average across 50 indentations. Using this data as a reference point the diameter of the pillar can be calculated at integers of 2a, 4a, 6a, 8a and 10a.

Circular cross-section pillars are milled into the surface of a [111] 5% pre-strained Nickel single crystal using the Focused Ion Beam (FIB) method perpendicular to the surface plane. The milling procedure implemented was of a 30KV accelerating voltage with a beam currents as high as 5nA for the initial milling stage and a final polishing step with beam currents of 49pA. The purpose of polishing at finer beam currents is that the tapering effect introduced by the milling process is reduced, negating any effects such as stress gradients.

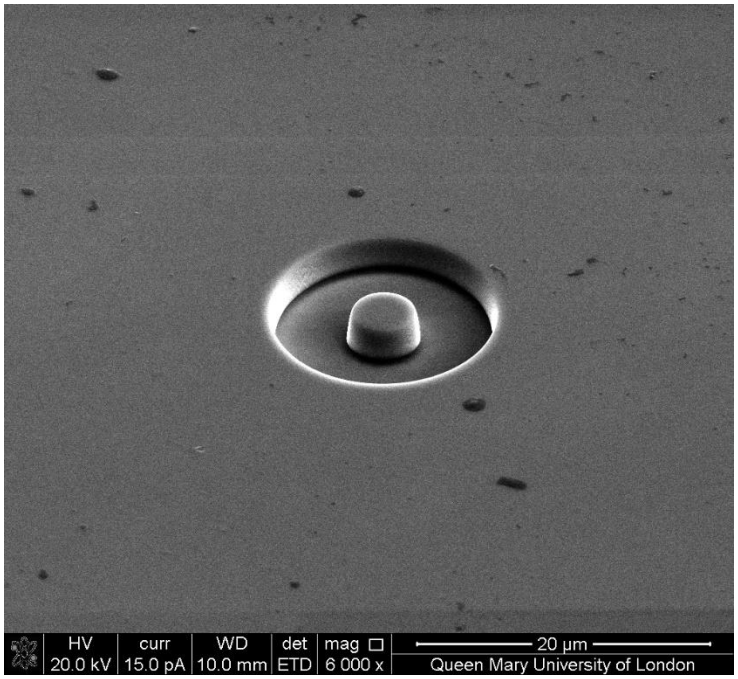

Figure 33: SEM imaging of a focused ion beam milled micropillar

The milling procedure implemented was of a 30KV accelerating voltage with a beam currents from 49pA to 5nA depending upon the magnitude of the pillar dimensions. Pillar diameters (D) in comparison with the radius of the indentation contact (a) vary in the region of $a < D < 10a$.Pillars are then indented using spherical diamond tip indenters with radii of 3.5µm and 5.0µm using a 75% partial unloading method. This allows a stress-strain curve to be generated showing the onset of plasticity. Validation of the contact between the indenter and the centre of the pillar takes place post indentation using high resolution imaging using SEM.

Calibration of the alignment of the indenter tip and microscope takes place before indentation of the pillars to ensure that the indenter tip makes contact at the centre of the pillar surface plane. Validation of the indentation process is carried out using SEM imaging.

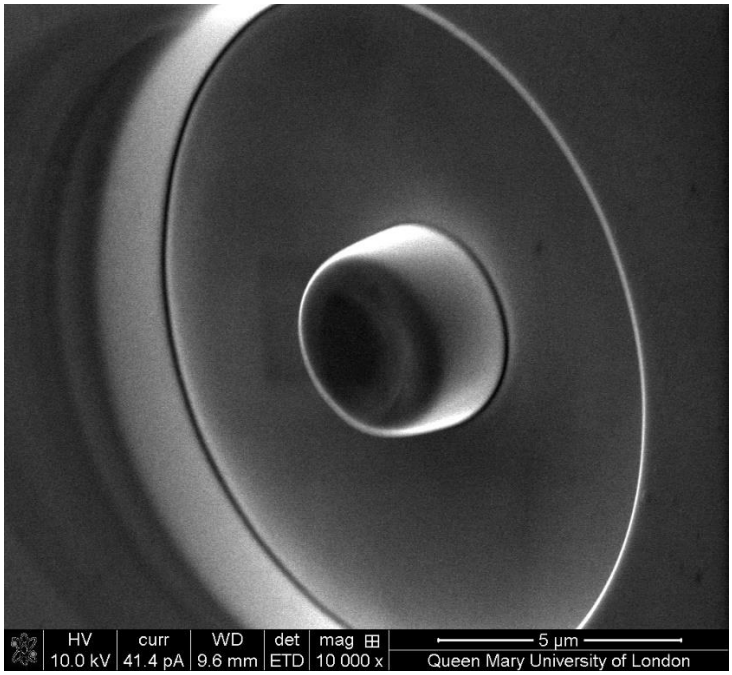

Figure 34: High resolution SEM imaging used to validate indentation

4.2 Results and Analysis

The indentation stress-strain response of the micropillars is presented in figures 35 and 36 The data is taken for specified contact sizes and indentation strain. The four a/R values are chosen to demonstrate the response and potential evolution of the plastic zone from post yielding (a/R=0.1) to significant plastic deformation with high dislocation density (a/R=0.35). The contact sizes for each subsequent a/R values for the 3µm and 5µm spherical tips are tabled below.

3µm Spherical tip				
a/R	0.1	0.15	0.25	0.35
Contact size (a)/ µm	0.35	0.5	0.82	1.2

Table 3: Contact sizes corresponding to indentation strain for 3µm spherical tip

5µm Spherical tip				
a/R	0.1	0.15	0.25	0.35
Contact size (a)/ µm	0.55	0.8	1.4	1.9

Table 4: Contact sizes corresponding to indentation strain for 5µm spherical tip

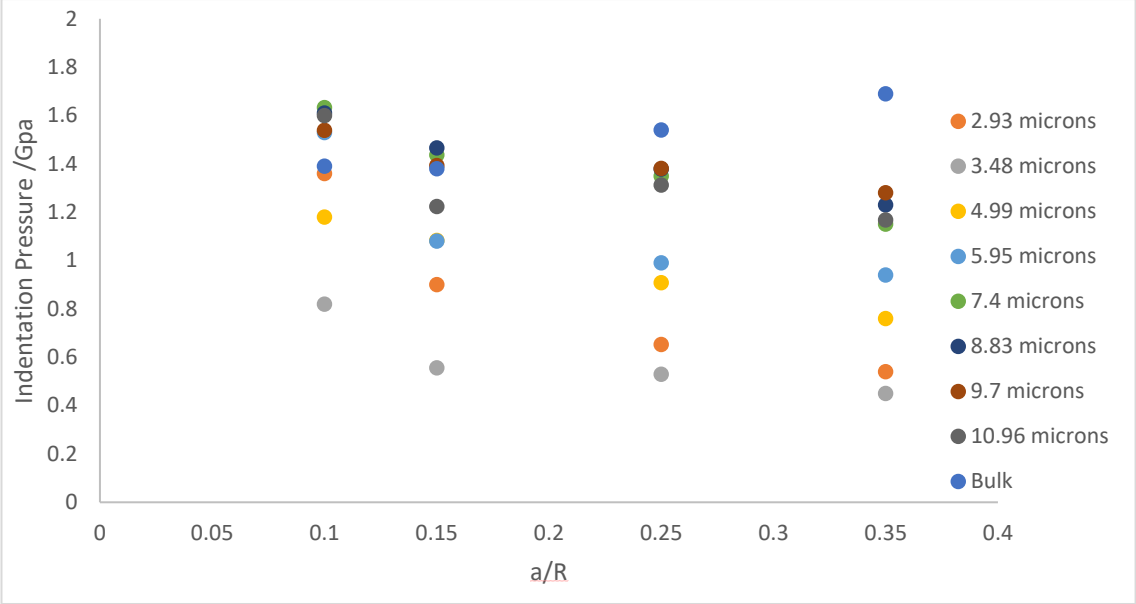

Figure 35: Indentation stress-strain data for 3µm spherical tip for varying pillar diameters

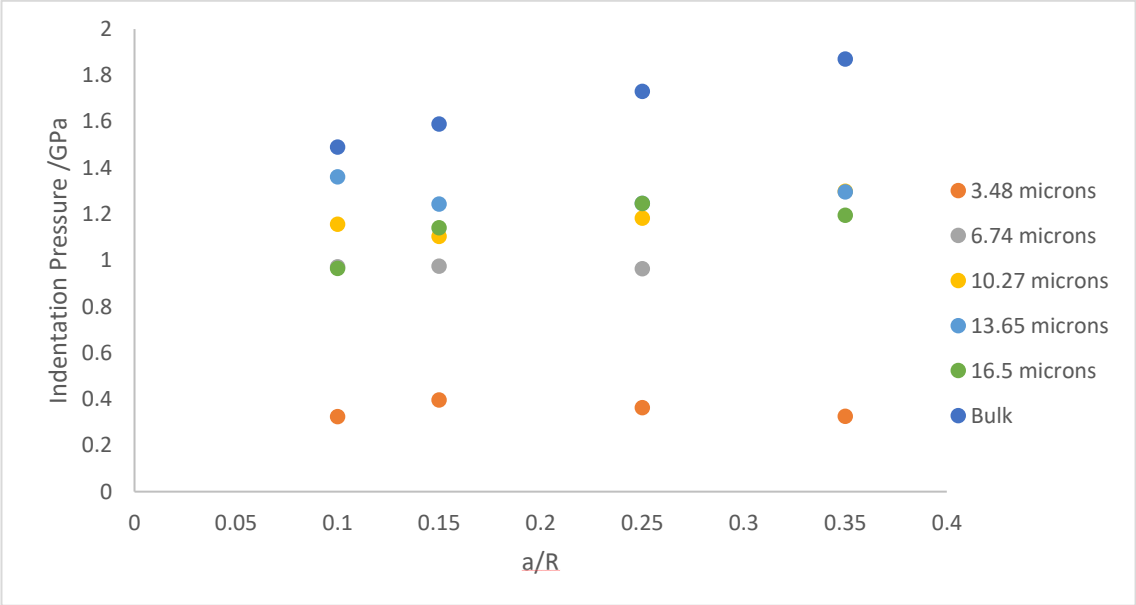

Figure 36: Indentation stress-strain data for 5µm spherical tip for varying pillar diameters

Figures 35 and 36 are selected data sets from the full range of pillar sizes for predetermined contact sizes, what is clearly demonstrated is the effect of the elastically constraining material on the mechanical response of the indentations. Reducing the potentially available elastically constrained material around the indentation supresses the indentation pressure post yield. This

is understandable as there is less potentially elastically strained material for the relieving of stress plastically. Not only is this attributed to the free surface but the increase in the pillar size in relation to the contact size is also attributed to the indentation size effect. Therefore, the assumption that the plastic zone size and its relationship to the contact size and by extension to the mechanical response is a valid one. The bulk data is also presented and is in keeping with our understanding of the effects of the elastically constraining material as the indentation pressure induced is above that or approximately equal to the indentation pressure for the largest pillars. Also of note is the absence of any significant strain hardening, in fact there are cases of strain softening. The experimental parameters of introducing a free surface so close to the area of deformation likely introduce processes of dislocation annihilation at the free surface boundary which may potentially lead to a dislocation starved state with in the micropillars. So, any increase in the indentation response seen thereafter may be the result of further dislocation nucleation processes. This has been argued but the data does not suggest this, it agrees more readily with the mechanism whereby only the dislocations outside the core are annihilated and those within the core pile-up at the core boundary. (Lian, Wang, Kim, & Greer, 2009)

Presented below in figures 37and 38 is the average indentation stress-strain data for 5% and 20% pre-strained single crystals. The reason for this comparison is to demonstrate the difference in the mechanical response in the two conditions. The crystals have been characterised and the dislocation densities calculated.

Sample	Cell Diameter (μm)	Dislocation density in cells (m-2)	Dislocation density on walls (m-2)	Total dislocation density (m-2)
5%	0.67 ± 0.23	9.7×10^{13}	6.5×10^{14}	3.7×10^{14}
20%	0.76 ± 0.50	2.3×10^{13}	1.1×10^{15}	4.5×10^{14}

Table 3: Dislocation density characterisation for 5% and 20% pre-strained Nickel single crystals

There is an apparent size effect, the 3μm and 5μm tips produce higher indentation stresses than the 20μm tip, as is expected. Of interest is that the 20μm tip has a higher strain hardening rate than the smaller tips and that the strain hardening rate of all the spherical tips is higher in the 20% pre-strained crystal. This is line with the finding of Schneider and Kiener et al, 2013 who argue that this is the effect of the dislocation cell walls in trapping mobile dislocations in a Taylor forest hardening like mechanism. It is because of the cell size in relation to the 20μm tip that this mechanism dominates only for the largest indenter. The reason for the higher strain hardening rate for the 20% data over the 5% data is obvious due to the higher total dislocation densities and requires no further clarification.

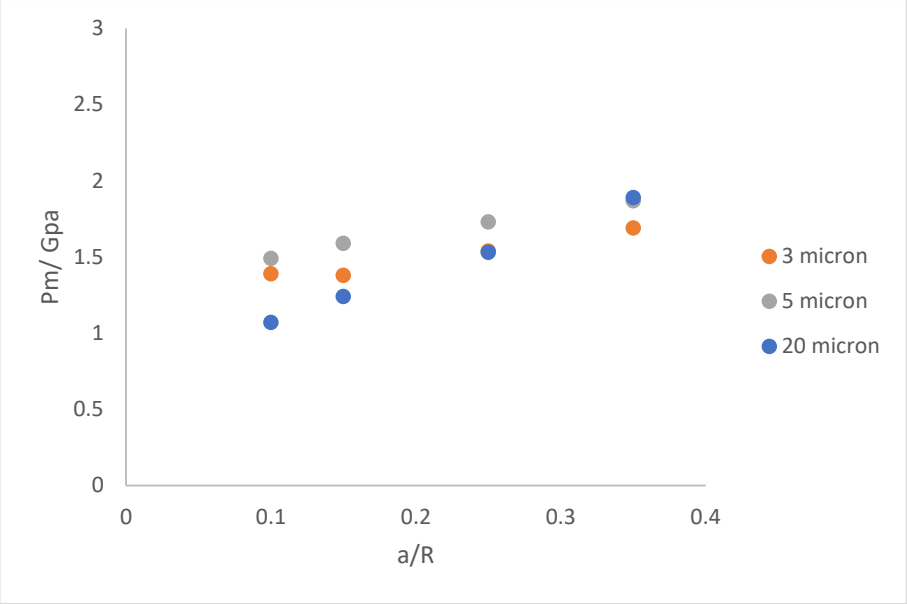

Figure 37: Averaged stress-strain responses for 3µm, 5µm and 20µm spherical tips indented in 5% pre-strained Nickel single crystal

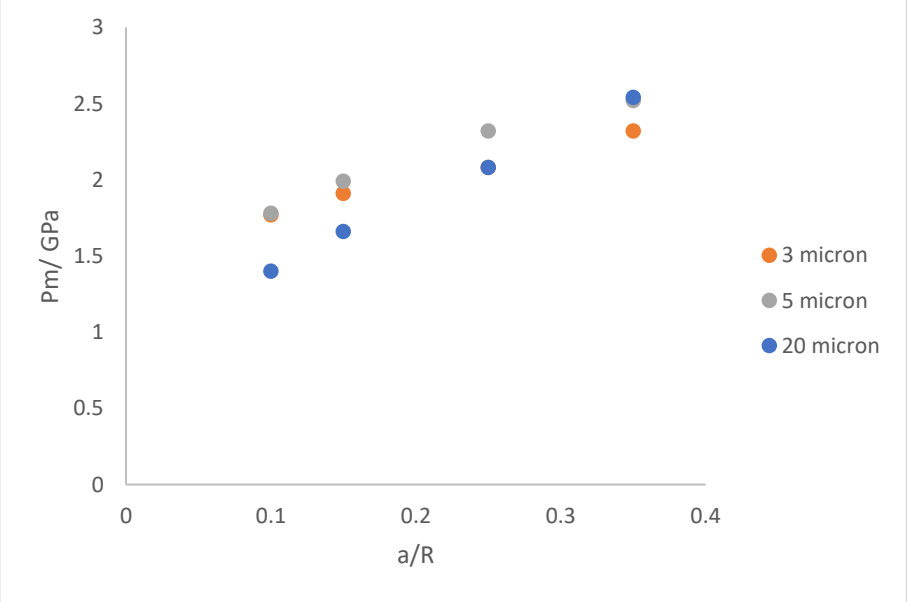

Figure 38: Averaged stress-strain responses for 3µm, 5µm and 20µm spherical tips indented in 20% pre-strained Nickel single crystal

To begin to determine the size of the plastic zone in relation to the diameter of the micropillars it is necessary to find the point at which the effect of the free surface becomes apparent. The indentation pressure (P_m) has been plotted against the ratio between twice the contact size and the pillar diameter (2a/D) (Figures 39 and 41). This plot allows for an analysis of the indentation

response of the plastic zone with changes in the elastically constrained material. The point of interest is taken to be a baseline indentation pressure dictated by the mechanical stress-strain data. This baseline indentation pressure is where the free surface begins to affect the response of the plastic zone. The baseline indentation pressure for the 3µm tip is approximately 0.5 GPa and for the 5µm is 0.4 GPa. This is of great interest because values of $\approx 400 - 500MPa$ fall in line with the compression data gathered previously on the same crystal. (Schneider, et al., 2013) It appears that the interaction between the plastic zone and the free surface changes the stress state within the pillar and begins to behave akin to a pillar under compression and not a pillar subject to hydrostatic forces.

The value 2a/D=0.3 corresponds to a contact size value of $\approx 0.5\mu m \; and \; \approx 0.55\mu m$ for the 3µm and 5µm tips respectively. If this assumption holds true for both sets of data this gives a 2a/D ratio of 0.3, giving a plastic zone size of 6a (figures 5-8). This agrees with well-established principles. This amounts to almost a confirmation that a higher flow stress is required at lower length scales to produce a plastic zone size of 6a. A larger data set containing a greater range of spherical tips would be required to confirm such assumptions. Coupling the data from figure 35, 36, 39 and 41 demonstrates that the indentation size effect becomes dominant when the structure size D is greater than 6 times the contact size $(D \gg 6a)$. A criticism that arises is, why does indentation pressure not fall instantly to what is coined the base indentation pressure upon reaching 2a/D the point that is argued to be the equilibrium point between the plastic zone and the pillar diameter? A reason for this could quite possible be that there is significant noise in the data or some uncertainty in the load-displacement or contact measurements. Or quite possibly be that the effect is only apparent from the onset of plasticity and bears no or little effect with subsequent evolution of the plastic zone. The changes in the stress field at the free surface may begin to progressively dictate the indentation response as a function of distance. The amalgamation of all the above is likely.

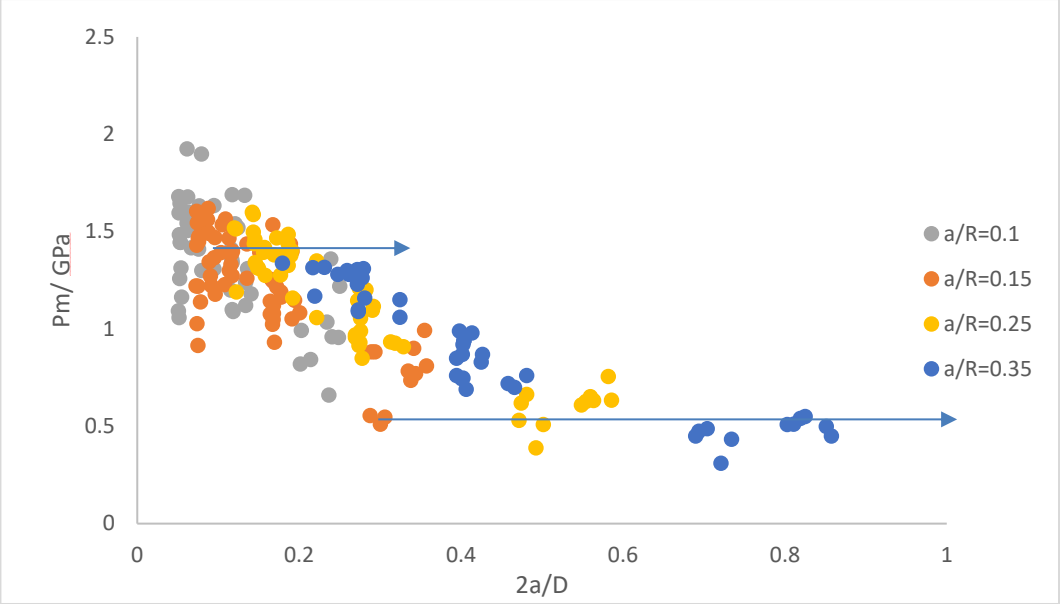

Figure 39: Indentation pressures at a/R values of 0.1, ,0.15, 0.25, and 0.35 for varying contact size to pillar diameter ratios for a 3µm spherical tip.

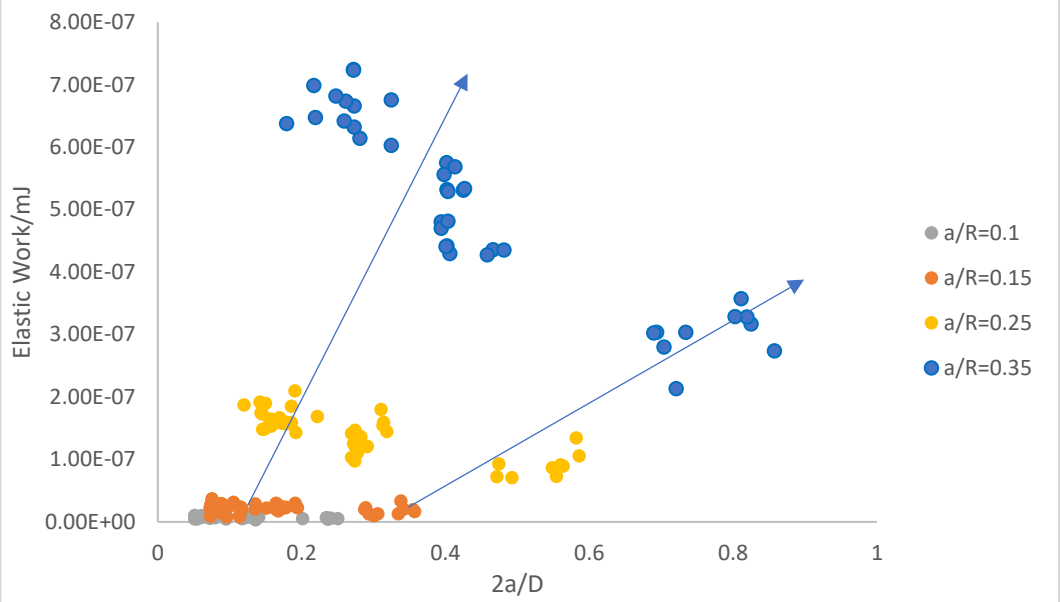

Figure 40: The elastic work done by 3µm tip at a/R values of 0.1, ,0.15, 0.25, and 0.35 for varying contact size to pillar diameter ratios, calculated using force-displacement loading data

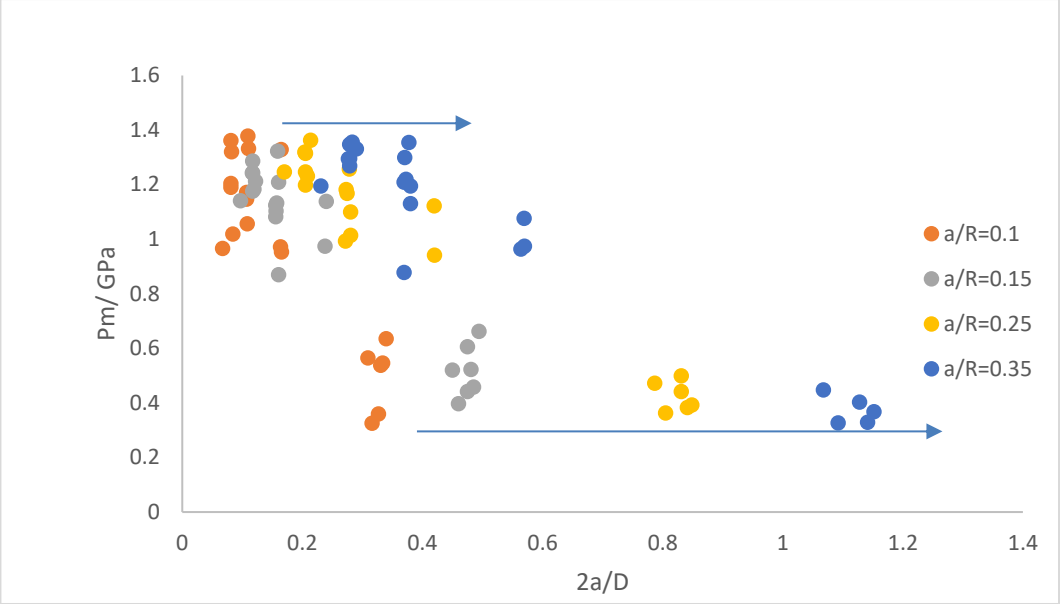

Figure 41: Indentation pressures at a/R 0.1, ,0.15, 0.25, and 0.35 for varying contact size to pillar diameter ratios for a 5µm spherical tip.

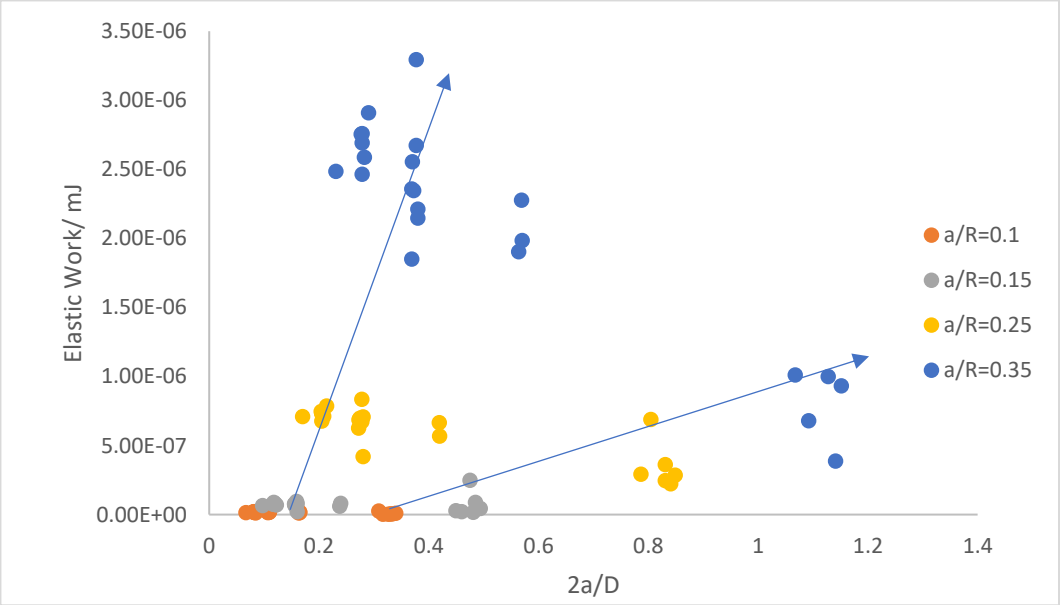

Figure 42: The elastic work done 5µm tip at a/R values of 0.1, ,0.15, 0.25, and 0.35 for varying contact size to pillar diameter ratios, calculated using force-displacement loading data

If the elastic energy is analysed alongside the indentation pressure data for 2a/D there is also an interesting trend in the energy data at 2a/D=0.3 (Figures 40 and 42). There appears to be a smaller incremental increase in the elastic work done as the contact size ratio to the pillar

diameter exceeds 0.3. This is likely due to the loss of constraint upon the plastic zone reflected in the drop in the indentation pressure. With the loss of the elastic constraint upon the plastic zone the indenter is required to do more work, meaning that in order to achieve the same development in the contact size less energy is required.

Below are the graphs showing the energy relieved plastically from the load displacement curves for the 3µm and 5µm tips presented in a logarithmic plot (Figures 43 and 44). The next question that arises is that does the internal energy relieved plastically corroborate the data presented earlier.

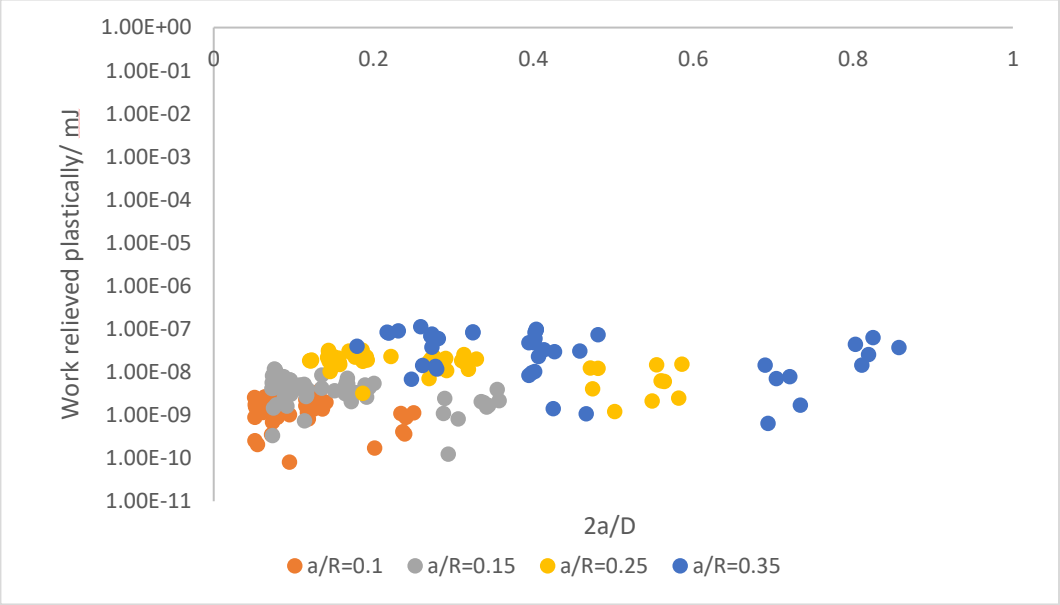

Figure 43: The energy relieved plastically by 3µm tip at a/R values of 0.1, ,0.15, 0.25, and 0.35 for varying contact size to pillar diameter ratios, calculated using force-displacement unloading data

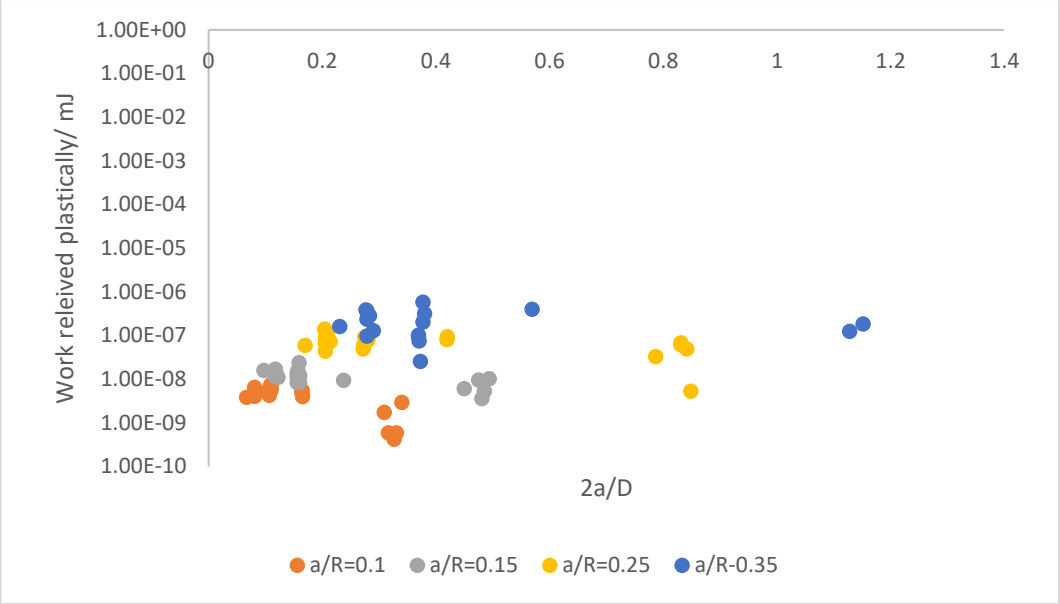

Figure 44: The energy relieved plastically by 5µm tip at a/R values of 0.1, ,0.15, 0.25, and 0.35 for varying contact size to pillar diameter ratios, calculated using force-displacement unloading data

The energy relieved plastically for a given value of a/R seems to all fall within an order of magnitude which is not surprising as the energy required to produce a plastic zone size of the same magnitude would require the same amount of energy relief. This is perhaps the strongest argument for the plastic zone size being constant regardless of the residual contact length scale at yielding. For those who dispute this based on imaging and mapping of plastic zones under indents using electron microscopy should perhaps consider the dislocation core and the plastic zone boundaries as separate but complimentary mechanisms of dislocation activity.

Conclusion

To conclude, the data suggests that the elastic work put into the system is independent of the plastic zone size because the energy required to produce a plastic zone of given size requires the same amount of energy relieved plastically (figures 43 & 44). The introduction of the constraint in the form of the free surface also shows little effect on the energy relieved plastically, thus implying a constant evolution of the plastic zone regardless of extrinsic material effects e.g. grain

boundaries and pillar edge. The size effect could be described as a materials ability to absorb elastic energy and more importantly its ability to relive energy plastically. This can be linked to the findings in this study which show that the ability to absorb elastic energy is tied to the propagation of the plastic zone and its interaction with the free surface. The introduction of a free surface is shown to impact the elastic work done. The plastic energy relieved is shown to be within an order of magnitude for any given indentation contact size, suggesting a coupling between the plastic energy relived and the plastic zone size. Using an understanding of the plastic zone interaction with a free surface and the coupling between the plastic energy relieved and its indentation contact size, may assist in our understanding of the factors driving the size effect and to which degree these factors are driving this phenomena.

Future work

This study has been far from comprehensive in in its outcomes on the subject of size effects. Naturally more work is required to build upon the findings in this thesis, by expanding micropillar indentation to a greater variety of single crystals, both metallic and ceramic. The range of length scales used requires further expanding to explore the onset of I.S.E and its manifestation in the nanometre range. I also believe that the nanoindentation of buried layers and multilayers will also be extremely beneficial in determining plastic zone size dimensions as a key length scale in size dependent strength.

Unfortunately, this study was unable to provide any images or mapping of plastic zones under spherical indentations. Although TEM, ECCI, EBSD, 3D-EBSD and TKD techniques were all attempted nothing materialised from this endeavour. The continuation of such experiments is recommended and is effective way of directly measuring plastic zone sizes while also being able characterise dislocations. Some images showing attempts are included in the appendix.

Appendix

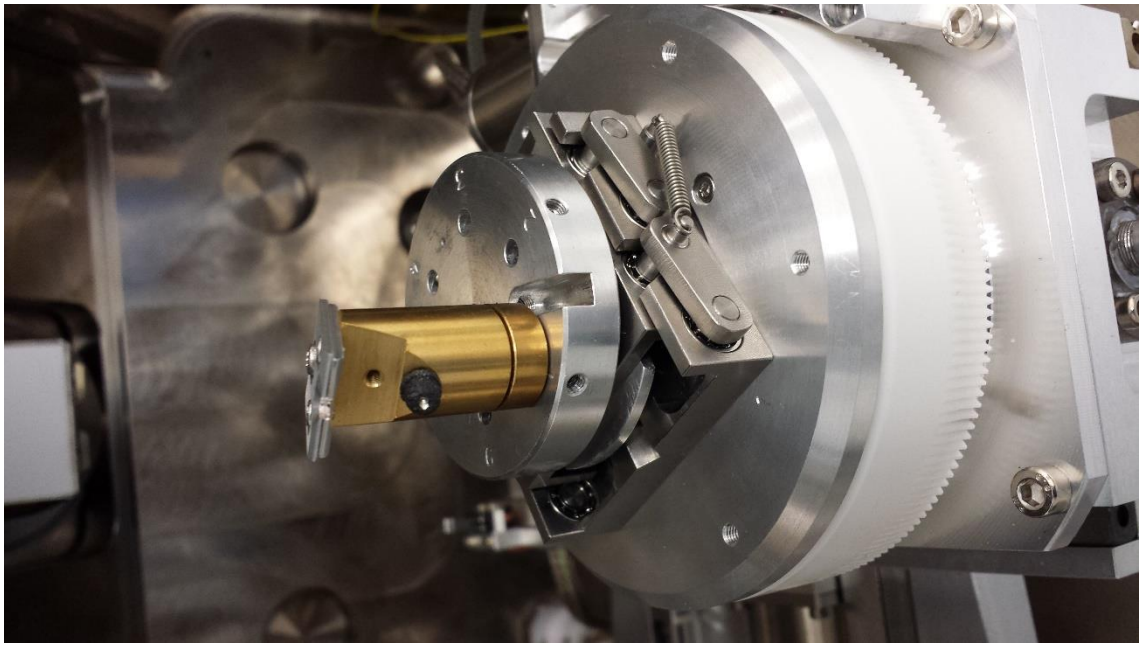

TKD set up in the SEM-FIB

Lift-out of lamellae for TEM imaging

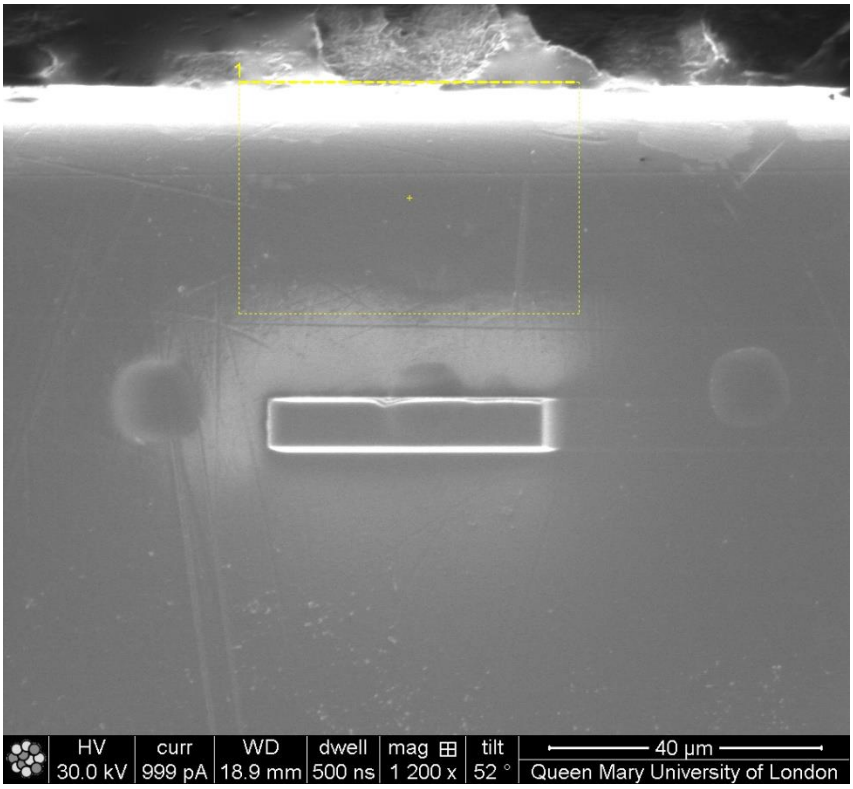

Sample preparation by milling a cross-section for 3D-EBSD mapping

References

Ashby, M. F. (1970). The Deformation of Plastically Non-homogeous Materials. *Philosophical Magazine, 21*(170), 399-421.

Barnoush, A. (2012). Correlation between dislocation density and nanomechanical response during nanoindentation. *Acta Materialia, 60*, 1268-1277.

Bei, H., Shim, S., Pharr, G. M., & George, E. P. (2008). Effects of pre-strain on the compressive stress–strain response of Mo-alloy single-crystal micropillars. *Acta Materialia, 56*, 4762–4770.

Brodusch, N., Demers, H., & Gauvin, R. (2013). Nanometres-resolution Kikuchi patterns from materials science specimens with transmission electron forward scatter diffraction in the scanning electron microscope. *Journal of Microscopy, 250*, 1-14.

Bushby, A. J. (2001). Nano-indentation using Spherical Indenters. *Nondestructive Testing and Evaluation , 17*, 213-234.

Bushby, A. J., & Jennett, N. M. (2001). Determining the Area Function of Spherical Indenters for Nanoindentation. *Material Research Society Symposium Proceedings. 649*, pp. Q7.17.1- Q7.17.6. San Francisco : Cambridge University Press.

Bushby, A. J., Zhu, T. T., & Dunstan, D. J. (2009, March). Slip distance model for the indentation size effect at the inititation of plasticity in ceramics and metals. *Journal of Materials Research, 24*(3), 966-972.

Carlton, C. E., & Ferreira, P. J. (2007). What is behind the Inverse Hall-Petch effect in Nanocrystalline Materials. *Acta Materialia, 55*, 3749-3756.

Cherkaoui, M., & Capolungo, L. (2009). *Atomistic and Continuum Modeling of Nanocrystalline Materials.* Springer, Boston, MA.

Chia, K., Jung, K., & Conrad, H. (2005). Dislocation density model for the effect of grain size on the flow stress of Ti-15.2% at % Mo B-alloy at 4.2-650K. *Material Science and Engineering A, 409*, 32-38.

Chokshi, A., Rosen, A., Karch, J., & Gleiter, H. (1989). On the Validity of the Hall-Petch Relationship in Nanocrystalline Materials. *Scripta Metallurgica, 23*, 1679-1683.

Conrad, H., & Jung, K. (2005a). Effect of grain size from millimeters to nanometers on the flow stress and deformation kinetics of Ag. *Material Science and Engineering A, 391*, 272-284.

Conrad, H., & Jung, K. (2005b). Effect of grain size from mm to nm on the flow stress and plastic deformation kinetics of Au at low homologous temperatures. *Material Science and Engineering A, 406*, 78-85.

Conrad, H., & Narayan, J. (2000). On the Grain Size Softening in Nanocrystalline materials. *Scripta Meterialia, 42*, 1025-1030.

Conrad, H., Feuerstein, S., & Rice, L. (1967, May). Effects of Grain SIze on the Dislocation Density and Flow Stress of Niobium. *Material Science and Engineering, 2*, 157-168.

Dunstan, D. J., & Bushby , A. J. (2014). Grain size dependence of the strength of metals: The Hall-Petch effect does not scale as the inverse square root of grain size. *International Journal of Plasticity, 53*, 56-65.

Dunstan, D. J., & Bushby, A. J. (2013). The scaling exponent in the size effect of small scale plastic deformation. *International Journal of Plasticity, 40*, 152-162.

Ehrler, B., Hou, X. D., Zhu, T. T., P'ng, K. Y., Walker, C. J., Bushby, A. J., & Dunstan, D. J. (2008, September). Grain size and sample size interact to determine strength in a soft metal. *Philosophical Magazine, 88*(25), 3043-3050.

Evans, A. G., & Hutchinson, J. W. (2009). A critical assessment of theories of strain gradient plasticity. *Acta Materialia, 57*, 1675-1688.

Field, J. S., & Swain, M. V. (1993, February). A simple predictive model for spherical indentation. *Journal of Materials Research, 8*(2), 297-306.

Fischer-Cripps, A. C. (2002). *Nanoindentation* (Second Edition ed.). New York: Springer.

Fischer-Cripps, A. C. (2010, May). The sharpness of a Berkovich indenter. *Journal of Materials Research, 25*(5), 927-934.

Fleck , N. A., Muller, G. M., Ashby, M. F., & Hutchinson, J. W. (1994). Strain gradient plasticity: Theory and Experiment. *Acta Metallurgica et Materialia, 42*(2), 475-487.

Fleck, N. A., Ashby, M. F., & Hutchinson, J. W. (2003). The role of geometrically necessary dislocations in giving material strengthening. *Scripta Metallurgica, 48*, 179-183.

Frick, C. P., Clark, B. G., Orso, S., Schneider, A. S., & Arzt, E. (2008). Size effect on strength and strain hardening of small-scale [1 1 1] nickel compression pillars. *Materials Science and Engineering A, 489*, 319-329.

Gao, H., & Huang, Y. (2003). Geometrically necessary dislocation and size-dependent plasticity. *Scripta Metallurgica , 48*, 113-118.

Gao, H., Huang, Y., Nix, W. D., & Hutchinson, J. W. (1999). Mechanism-based strain gradient plasticity - 1. Theory. *Journal of the Mechanics and Physics of Solids, 47*, 1239-1263.

Geisse, R. H., Rice, K. P., & Keller, R. R. (2013, May). Transmission EBSD in the Scanning Electron Microscope. *Microscopy today, 21*(3), 16-20. doi: http://dx.doi.org/10.1017/S1551929513000503

Goldstein, J. I., Newbury, D. E., Echlin, P., Joy, D. C., Romig, A. D., Lyman, C. E., . . . Lifshin, E. (1992). *Scanning Electron Microscopy and X-Ray Analysis* (second edition ed.). New York: Plenum Press.

Greer, J. R., & De Hosson, J. T. (2011). Plasticity in small-sized metallic systems: Intrinsic versus extrinsic size effect. *Progress in Materials Science, 56*, 654–724.

Greer, J. R., & Nix , W. D. (2006). Nanoscale gold pillars strengthened through dislocation starvation. *Physical Review B, 73*, 245410-1 - 245410-6.

Greer, J. R., Oliver, W. C., & Nix, W. D. (2005). Size dependence of mechanical properties of gold at the micron. *Acta Materialia, 53*, 1821–1830.

Greer, J. R., Weinberger, C. R., & Cai, W. (2008). Comparing the strength of f.c.c. and b.c.c. sub-micrometer pillars: Compression experiments and dislocation dynamics simulations. *Materials Science and Engineering A, 493*, 21-25.

Gutierrez-Urrutia, I., & Raabe, D. (2012). Dislocation density measurement by electron channeling contrast imaging in scanning electron microscope. *Scripta Materialia, 66*, 343-346.

Hall, E. (1951, March 8). The deformation and ageing of mild steel: 3 Discussion of results. *Proc. Phys. Soc. B, 64*, 747-753.

Herrmann, K., Jennett, N. M., Wegener, W., Meneve, J., Hasche, K., & Seeman, R. (2000). Progress in determination of the area function of indenters used for nanoindentation. *Thin Solid Films, 377-378*, 394-400.

Hou, X. D., & Jennett, N. M. (2012). Application of a modified slip-distance theory to the indentation of single-crystal and polycrstalline copper to model the interactions between the indentation size and structure size. *Acta Materialia, 60*, 4128-4135.

Hou, X. D., Bushby, A. J., & Jennett, N. M. (2008). Study of the interaction between the indentation size effect and the Hall-Petch effect with spherical indenters on annealed polycrystalline copper. *Journal of Physics D: Applied Physics, 41*, 1-7.

Jennett, N. M., Ghisleni, R., & Michler, J. (2009). Enhanced yield strength of materials: The thinness effect. *Applied Physics Letters, 95*, 123102-1 - 123102-3.

Jennett, N. M., Hou, X., & Parlinska, M. (2012). Exploiting interactions between structure size and indentation size effects to determine the charcteristic dimension of nano-structured materials by indentation. *Submitted 2012*, 1-12.

Johnson, K. L. (1985). Hertz theory of elastic contact. In K. L. Johnson, *Contact Mechanics* (pp. 90-106). Cambridge University Press.

Kaboli, S., Goldbaum, D., Chromik, R. R., & Gauvin, R. (2013). Electron Channeling Contrast Imaging of Plastic Deformation Indced by Indentation in Polycrystalline Nickel. *Microscopy and Microanalysis, 19*, 1620-1631.

Keller, R. R., & Geiss, R. H. (2012). Transmission EBSD from 10 nm domains in a scanning electron microscope. *Journal of Microscopy, 245*, 245-251.

Li, J. (1963a, February). Petch Relationship and Grain Boundary Sources. *Transactions of the Metallurgical Society of AIME, 227*, 239-247.

Li, J. (1963b, May). Some Dislocation Mechansisms in Deformation, Recovery and Recrystallisation of Metals. *The Journal of the Australian Institute of Metals, 8*(2), 206-221.

Li, J., & Chou, Y.T. (1970, May). The Role of Dislocations in the Flow Stress Grain Size Relationship. *Metallurgical Transactions, 1*, 1145-1158.

Li, Y., Bushby, A. J., & Dunstan, D. J. (2014). The Hall-Petch effect as a manifestation of the general size effect. *Presented at Symposium on Plasticity 2014*, 1-33.

Lian, J., Wang, J., Kim, Y., & Greer, J. (2009). Sample boundary effect in nanoindentation of nano and microscale surface structures. *Jopurnal of the mechanics and physics of solids, 57*, 812-827.

Lim, Y. Y., & Chaudhri, M. M. (1999). The effect of the indenter load on the nanohardness of ductile metals: An experimental stufy on polycrystyalline work-hardened and annealed oxygen-free copper. *Philosophical Magazine A, 79*(12), 2979-3000.

Lim, Y. Y., Bushby, A. J., & Chaudhri, M. M. (1998). Nano and Macro Indentation Studies of Polycrystalline Copper using Spherical Indentation. *Mateirials Research Society Symposium Proceedings, 522*, 145-150.

Liu, D., & Dunstan, D. J. (2017). Material length scale of strain gradient plasticity: A physical interpretation. *International journal of plasticity*, 1-19. Retrieved from http://ac.els-cdn.com/S0749641917301559/1-s2.0-S0749641917301559-main.pdf?_tid=8ca2acea-9894-11e7-99c2-00000aab0f6b&acdnat=1505315124_b3fff419e8a6a1626a74757346ee07d4

Ma, L., & Levie, L. E. (2007, June). Effect of the spherical tip assumption on nanoindentation. *Journal of Materials Research, 22*(6), 1655-1661.

Ma, Q., & Clarke, D. R. (1995, April). Size dependent hardness of silver single crystals. *Journal of Materials Research, 1*-(4), 853-863.

Murr, L. (1975, March). Some Observation of Grain Boundary Ledges and Ledges as Dislocation Sources in Metals and Alloys. *Metallurgical Transactions, 6*, 505-513.

Ng, K. S., & Ngan, A. H. (2009). Effects of trapping dislocations within small crystals on their deformation behavior. *Acta Materialia, 57*, 4902–4910.

Niordson , C. F., & Hutchinson, J. W. (2011). Basic strain gradient plasticity theories with application to constrained film deformation. *Journal of mechanics of materials and structures, 6*(1-4), 395-416.

Nix, W. D., & Gao, H. (1998). Indentation Size Effects in Crystalline Materials: A Law for Strain Gradient Plasticity. *Journal of the Mechanics and Physics of Solids, 46*(3), 411-425.

Oliver, W. C., & Pharr, G. M. (1992, June). An improved technique for determining hardness and elastic modulus using load and displacement sensing indentation experiments. *Journal of Materials Research, 7*(6), 1564-1583.

Petch, N. (1953, May). The cleavage strength of polycrystals. *Journal of the Iron and Steel Institte, 174*, 25-28.

Pharr, G. M., Herbert, E. G., & Goa, Y. (2010). The Indentation Size Effect: A Critical Examination of Experimental Observations and Mechanistic Interpretation. *The Annual Review of Materials Research, 40*, 271-292.

Pharr, G. M., Oliver, W. C., & Brotzen, F. R. (1992b, March). On the generality of the relationship among contact stiffness, contact area, and elastic modulus during indentation. *Journal of Materials Research, 7*(3), 613-317.

Rice, K. P., Keller, R. R., & Stoykovich, M. P. (2014). Specimen-thickness effects on transmission Kikuchi patterns in the scanning electron microscope. *Journal of Microscopy, 254*(3), 129-136.

Schneider, A. S., Kiener, D., Yakacki, C. M., Maier, H. J., Gruber, P. A., Tamura, N., . . . Frick , C. P. (2013). Influence of bulk pre-straining on the size effect in nickel compression pillars. *Material Science and Engineering A, 559*, 147-158.

Shan, Z. W., Mishra, R. K., Syed Asif, S. A., Warren , O. L., & Minor, A. M. (2008). Mechanical annealing and source-limited deformation in submicrometre-diameter Ni crystals. *nature materials, 7*, 115-119.

Simkin, B. A., & Crimp, M. A. (1999). An experimentally convenient configuration for electron channeling contrast imaging. *Ultramicroscopy, 77*, 65-75.

Spary, I. J., Bushby, A. J., & Jennett, N. M. (2006). On the indentation size effect in spherical indentation. *Philosophical Magazine, 86*(33-35), 5581-5593.

Swadener, J. G., George, E. P., & Pharr, G. M. (2002). The correlation of the indentation size effect measured with indenters of various shapes. *Journal of Mechanics and Physics of Solids, 50*, 681-694.

Trimby, P. K., Cao, Y., Chen, Z., Han, S., Hemker, K. J., Lian, J., . . . Cairney, J. M. (2014). Characterizing deformed ultrafine-grained and nanocrystalline materials using transmission Kikuchi diffraction in a scanning electron microscope. *Acta Materialia, 62*, 69-80.

Trimby, P. W. (2012). Orientation mapping of nanostructured materials using transmission Kikuchi diffraction in the scanning electron microscope. *Ultramicroscopy, 120*, 16-24.

Trimby, P. W., & Cairney, J. M. (2014, February). Transmission Kikuchi Diffraction in the Scanning Eletron Microscope: Orientation Mapping on the Nanoscale. *Advanced Materials and Processes*, 13-15.

Uchic , M. D., Shade, P. A., & Dimiduk, D. M. (2009). Plasticity of micro-scale single crystals in compression. *Annual Review of Materials Research, 39*, 361-386.

Uchic, M. D., Dimiduk, D. M., Florando, J. N., & Nix , W. D. (2004B). Sample dimension influence strength and crystal plasticity. *Science, 305*, 986-989.

Uchic, M. D., Dimiduk, D. M., Florando, J. N., & Nix, W. D. (2002). Exploring specimen size effects in plastic deformation of Ni3(Al, Ta). *MRS Proceedings, 753*, BB1.4.1- BB1.4.6.

Uchic, M. D., Dimiduk, D. M., Florando, J. N., & Nix, W. D. (2004). Sample dimension inflence strength and crystal plasticty. *Science, 305*, 986-989.

Weertman, J. R. (1993). Hall-Petch strengthening in nanocrystalline metals. *Material Science and Engineering A, 166*, 161-167.

Welsch, M. T., Henning, M., Marx, M., & Vehoff, H. (2007). Measuring the Plastic ZOne Size by Orientation Gradient Mapping (OGM) and Electron Channeling Contrast Imaging (ECCI). *Advanced Engineering Materials, 9*(1-2), 31-37.

Williams, D. B., & Carter, C. B. (2009). *Transmission Electrom Microscopy: A textbook for materials science* (second edition ed.). New York: Springer.

Zaefferer, S., & Elhami, N. N. (2014). Theory and application of electron channelling contrast imaging under controlled diffraction conditions. *Acta Materialia, 75*, 20-50.

Zaefferer, S., Elhami, N. N., & Gutierrez, I. (2011). *Defect Observation by Electron Channeling Contrast Iaging (ECCI) under Controlled Diffraction Conditions in the Scanning Electron Microscope.* Retrieved February 05, 2014, from Max Planck Institute: http://www.mpie.de/index.php?id=3542&L=1fileadmin%2Ftemplates%2FMPIE%2Fimages%2Fminerva_logo.gif&type=1

Zhang, J. I., Zaefferer, S., & Raabe, D. (2015). A study on the geometry of dislocation patterns in the surrounding of nanoindents in a TWIP steel using electron channeling contrast imaging and discrete dislocation dynamics simulation. *Materials Science & Engineering A, 636*, 231-242.

Zhu, T. T., Bushby, A. J., & Dunstan, D. J. (2008a). Size Effect in the initiation of plasticity for ceramics and metals. *Journal of the Mechanics and Physics of Solids, 56*, 1170-1185.

Zhu, T. T., Hou, X. D., Bushby, A. J., & Dunstan, D. J. (2008b). Indentation size effect at the initiation of plasticity for ceramics in nanoindentation. *Journal of Physics D: Applied Physics, 41*, 1-6.